

FlexRT - A fast and flexible cosmological radiative transfer code for reionization studies I: Code validation

Christopher Cain^a and Anson D'Aloisio^b

^aSchool of Earth and Space exploration, Arizona State University, Tempe, AZ 85281, USA

^bDepartment of Physics and Astronomy, University of California, Riverside

E-mail: clcain3@asu.edu, ansond@ucr.edu

Abstract. The wealth of high-quality observational data from the epoch of reionization that will become available in the next decade motivates further development of modeling techniques for their interpretation. Among the key challenges in modeling reionization are (1) its multi-scale nature, (2) the computational demands of solving the radiative transfer (RT) equation, and (3) the large size of reionization's parameter space. In this paper, we present and validate a new RT code designed to confront these challenges. FLEXRT (Flexible Radiative Transfer) combines adaptive ray tracing with a highly flexible treatment of the intergalactic ionizing opacity. This gives the user control over how the intergalactic medium (IGM) is modeled, and provides a way to reduce the computational cost of a FLEXRT simulation by orders of magnitude while still accounting for small-scale IGM physics. Alternatively, the user may increase the angular and spatial resolution of the algorithm to run a more traditional reionization simulation. FLEXRT has already been used in several contexts, including simulations of the Lyman- α forest of high- z quasars, the redshifted 21cm signal from reionization, as well as in higher resolution reionization simulations in smaller volumes. In this work, we motivate and describe the code, and validate it against a set of standard test problems from the Cosmological Radiative Transfer Comparison Project. We find that FLEXRT is in broad agreement with a number of existing RT codes in all of these tests. Lastly, we compare FLEXRT to an existing adaptive ray tracing code to validate FLEXRT in a cosmological reionization simulation.

¹Corresponding author.

Contents

1	Introduction	1
2	The context & motivation for FLEXRT	4
2.1	Radiative transfer implementations	4
2.1.1	Moment-Based RT methods	4
2.1.2	Ray-tracing	5
2.1.3	Monte-Carlo methods	6
2.2	Features of FLEXRT & their motivation	6
2.2.1	The RT method of choice for FLEXRT	6
2.2.2	Small-scale IGM physics	6
3	Adaptive Ray Tracing Implementation	7
3.1	Ray creation and propagation	7
3.2	Ray splitting	8
3.3	Ray merging	8
4	Treatments of the IGM Opacity	9
4.1	Direct solution of the chemistry equations (“Standard Mode”)	10
4.2	General treatment (“Generalized Opacity Mode”)	12
5	Cosmological RT Comparison Project (2006) Tests	16
5.1	Iso-thermal Stromgren Sphere (Test #1)	16
5.2	Stromgren sphere with T evolution (Test #2)	20
5.3	I-front trapping by a dense clump (Test #3)	22
5.4	Test with Cosmological Sources (Test #4)	27
6	Validity of the Moving-Screen I-front method	29
7	Testing the Merging Scheme	31
7.1	CRTCP Test #4 (again)	31
7.2	Test against RADHYDRO	32
8	Conclusions	40

1 Introduction

The Epoch of Reionization (EoR) lies at the forefront of current and forthcoming observational efforts. In its first cycles, JWST has already begun to study galaxies and active galactic nuclei (AGN) throughout the EoR ($6 \lesssim z \lesssim 15$) in unprecedented detail, including their intrinsic ionizing properties [1–5]. Ongoing and future cosmic microwave background (CMB) experiments such as the Atacama Cosmology Telescope (ACT; [6]), South Pole Telescope (SPT; [7]), Simons Observatory [8], and CMB-S4 [9] will use the patchy kinetic Sunyaev Zel’dovich (kSZ) and τ_{es} effects to place tighter limits on the timing and duration of reionization. Over the next decade, 21cm experiments such as the Hydrogen Epoch of Reionization

Array (HERA; [10]) and the Square Kilometre Array (SKA; [11]) will continue to improve existing upper limits [e.g. 12, 13] and possibly detect the EoR signal for the first time.

Meanwhile, quasar absorption spectra measurements have advanced our understanding of the reionization history substantially, especially for the last phases of reionization. The tail end of reionization has likely been detected in the statistics of the $5 < z < 6$ Ly α forest, e.g. the mean flux evolution, large-scale τ_{eff} fluctuations, and dark gap statistics [14–19]. The rapid evolution in the ionizing photon mean free path observed at $z > 5.5$ is also consistent with the tail of reionization [20–25]. These measurements provide important boundary conditions that must be obeyed by any successful reionization model. Additionally, the presence of damping wings in $z > 6$ quasar spectra help constrain the global neutral fraction at higher redshift [e.g. 26, 27]. Quasar absorption spectra will continue to play a prominent role in studying reionization because the number of high-quality quasar spectra will soon grow substantially. Cosmological surveys by the Vera Rubin Observatory and the Dark Energy Spectroscopic Instrument (DESI) are projected to discover more than 10,000 $z > 6$ quasars [28, 29], some fraction of which will be followed up with high-resolution spectrographs. Most recently, signs of damping wing absorption in the $z < 6$ Ly α forest have strengthened the hypothesis that reionization is ongoing at these redshifts [30, 31].

Looking forward, the deepest insights into reionization will come from combining these rich and complimentary data sets. A key problem confronting the field is how to maximize the information contained in them. Together, they are broadly sensitive to not only the distribution of intergalactic hydrogen during reionization, but also the structures and histories of the HI-ionizing radiation background and IGM temperature. Simulating reionization accurately at this level of detail requires solving, or at least approximating, the radiative transfer (RT) equation, which encodes the physics linking the ionizing sources to the state of the IGM. But solving the RT equation in this context is a formidable computational challenge for several reasons. The first is the high dimensionality of the problem. The RT equation has 7 dimensions (3 spatial, 2 angular, 1 frequency, and 1 time), all of which are important for reionization. Moreover, reionization is a massively multi-scale problem. The intrinsic ionizing properties of galaxies are set by astrophysics on parsec scales and below: star formation and feedback processes, AGN activity, as well as the structures of the interstellar and circumgalactic media. The small-scale clumpiness of the IGM sets its recombination rate and self-shielding properties, which determine the number of photons that the sources must produce to complete reionization [32–34]. The clumping scale may be as low as a kpc. Finally, simulations in representative volumes (10s-100s of cMpc on a side) may also contain millions of ionizing sources clustering on ~ 10 cMpc scales. The distribution and sizes of ionized regions depends on the source clustering as well as the small-scale clumpiness of the IGM [e.g. 35]. In principle, therefore, reionization simulations require at least 8 – 9 orders of magnitude in dynamic range to bridge the gap between galaxy physics (on \sim parsec scales) and the large-scale features of reionization.

Because it is impossible to fully resolve every process relevant for reionization, the problem also consists of many dimensions *in parameter space*. Most free parameters typically characterize the highly uncertain ionizing outputs of the sources, e.g. the ionizing escape fraction, which may in general depend on galaxy properties and redshift. Indeed, constraining the source parameters is a chief goal of the field, since they are often very challenging or otherwise impossible to study directly. The opacity of the ionized IGM to ionizing photons is also frequently treated as a free parameter, parameterized by either a mean free path (MFP) or a recombination clumping factor [36–38]. The most recent parameter inference studies

include $\sim 5 - 10$ free parameters, requiring thousands to millions of simulations [e.g. 39, 40].

Owing to these difficulties, reionization simulations are divided into two very different approaches, broadly speaking. One approach avoids the computational cost of explicitly solving the RT equation, using instead numerical recipes that approximate the most important facets of the full RT solution. These are often referred to as “semi-numerical” methods and are designed for probing the vast parameter space of reionization [e.g. 41–45]. The second approach, which we call “fully numerical,” is to solve the RT equation in detailed cosmological simulations using methods that take advantage of simplifications and/or optimizations afforded by the unique nature of the reionization problem [46–52].

Of course, both approaches have their advantages and disadvantages, which largely dictate their uses. Semi-numeric codes can well-approximate the solution of the RT equation in the context of reionization [53]. Parameter space inferences are impossible without them. However, because these algorithms do not solve the RT equation, they do not converge to the exact RT solution; improving their accuracy is not simply a matter of increasing the number of resolution elements. As such, quantifying their modeling errors can be a difficult task. Additionally, these methods are less suited to modeling the ionizing radiation background and IGM temperature – both critical elements for modeling quasar absorption spectra (see however [16] and [39, 54] for prescriptions along these lines.)

On the other hand, the fully numerical approach is well-suited for studying in detail the state and physics of the reionizing IGM. In recent years, this approach has generally moved in the direction of fully coupled radiative hydrodynamics simulations, many of which also simulate the galaxies, including star formation, AGN, and feedback processes [e.g. 49, 51, 52, 55, 56]. With this comes the great advantage that the simulations can now leverage the constraints provided by direct observations of the galaxy population. But the state-of-the-art simulations can cost millions of core hours per run, allowing for only a handful of simulations to be run per year, which precludes parameter space studies. The limited number of such simulations available also makes it difficult to disentangle the effects of approximations and differing sub-grid modeling choices, which are required in even the most state-of-the-art simulations [e.g. 57, 58]. It is also worth noting that the moment-based RT methods that are most widely used today truncate the moment hierarchy at the dipole moment of the intensity field by making an ansatz for the quadrupole, and therefore start from an approximate form of the RT equation. Hence, these methods also do not converge to the exact RT solution in any limit of the parameters related to numerical implementation (e.g. number of resolution elements).

We have been developing a new RT code named FLEXRT (short for Flexible Radiative Transfer) that attempts to achieve some of the speedup afforded by semi-numeric methods without losing direct contact with the RT equation. The organizing principle of FLEXRT is flexibility for the user to tune the level of fidelity up or down as needed for the problem at hand. Our code solves the RT equation directly, so it converges, at least in principle, to the exact solution in the limit of infinitely many resolution elements. This allows modeling errors associated with the RT to be straightforwardly quantified. We also aim for the code to be sufficiently fast (in the regime of fewer resolution elements) and accurate enough for modestly-sized parameter space studies. To achieve this, FLEXRT has two central features: (1) an adaptive ray tracing scheme with numerical parameters that can be adjusted to trade off the speed and accuracy of the RT calculation as desired, and (2) a highly flexible, general prescription for the intergalactic ionizing photon opacity that admits the use of a wide variety of models for un-resolved IGM dynamics. This allows FLEXRT to increase the effective

dynamic range of the simulation without requiring more RT cells.

The first iteration of FLEXRT has already been used in several studies [e.g. 21, 35]. In this first paper of a multi-part series, we will describe FLEXRT’s basic framework in detail and present a battery of tests validating its basic functionality and accuracy. In Paper II, we will present a new and improved version of the sub-grid opacity model first described in Ref. [21], and demonstrate its accuracy in capturing the effects of un-resolved IGM physics down to \sim kpc scales. Paper III will present performance tests of a further optimized version of FLEXRT and demonstrate its use in a simple parameter-space study.

This work is outlined as follows. In §2, we briefly summarize several of the radiative transfer methods widely used in reionization studies, and describe how FLEXRT fits into this context. §3 describes the ray tracing approach used in FLEXRT, while §4 describes how we solve for the IGM opacity and the ionization state of the gas. In §5, we subject FLEXRT to the static density RT tests outline in the Cosmological Radiative Transfer Codes Comparison Project [Paper I, 59]. §6 addresses how FLEXRT handles the propagation of cosmological ionization fronts. In §7, we run additional tests that target the ray tracing method used in FLEXRT, including a direct test against the RADHYDRO code of Ref. [47]. We conclude in §8. Throughout, we assume the following cosmological parameters: $\Omega_m = 0.305$, $\Omega_\Lambda = 1 - \Omega_m$, $\Omega_b = 0.048$, $h = 0.68$, $n_s = 0.9667$ and $\sigma_8 = 0.82$, consistent with results from Ref. [60]. All distances are quoted in co-moving units unless otherwise specified.

2 The context & motivation for FLEXRT

In this section, we briefly summarize the landscape of existing radiative transfer methods used to simulate reionization. These include moment-based (§2.1.1), ray-tracing (§2.1.2), and Monte-Carlo methods (§2.1.3). This section is not a comprehensive summary; rather, it aims to establish context and motivation for FLEXRT. Readers interested in the details of FLEXRT may skip this section without loss of continuity.

2.1 Radiative transfer implementations

2.1.1 Moment-Based RT methods

The high dimensionality of the RT equation makes it one of the most computationally intensive equations to solve numerically, even in relatively simple cases. A common approach to reducing the dimensionality is to take moments of the RT equation in the angular dimensions, and then truncate the hierarchy at the dipole level with an ansatz for the quadrupole moment, i.e. the Eddington tensor. The two most prominent ansatzes in use for reionization codes today are the M1 closure [61] and the optically thin Eddington tensor [OTVET; 62]. The equations governing the first two moments – the radiation energy density and flux – take on the form of conservation laws, analogous to the Euler equations of fluid dynamics, for which very efficient numerical solvers have been developed. Such codes are also relatively straightforward to parallelize across many CPUs because of their fluid-like description of the radiation field. Indeed, the M1 closure has the particularly convenient property that the Eddington tensor becomes a local function of radiation energy density and flux. Owing to its computational efficiency, the moment approach has become the most widely adopted type of RT algorithm used in almost all of the recent radiation hydrodynamics simulations of reionization, many of which include galaxy formation physics [49–52, 55]. Indeed, without the moment-based RT implementations, the unprecedented scales and resolutions achieved by these simulations would not be possible.

The accuracy of moment-based codes has been quantified for a suite of idealized test problems in the Cosmological Radiative Transfer Comparison Project [59, 63], and in other works [e.g. 48, 64]. To our knowledge, however, there has been no quantitative study on the inaccuracies introduced by the fluid-like approximation to the radiation field, which arises from the local approximation to the Eddington tensor in the M1 method, in the cosmological reionization problem. There is good motivation for such a study. Ref. [65] considered several idealized RT problems that are relevant for reionization and found that moment-based methods tend to: (1) over-ionize dense, self-shielding absorption systems, which can result in a factor of ~ 2 under-prediction of the photoionization rate of intergalactic gas for a given emissivity; and (2) err in the structure of the ionizing radiation background on scales smaller than the mean free path (MFP). For instance, they found that the M1 closure significantly underestimates the fluctuations on these scales. This effect is visualized nicely in Figure 5 of Ref. [23], who noted that RT simulations run with ATON broadly exhibited a more uniform ionizing background compared to models generated with EX-CITE, which is essentially a ray tracing algorithm.

In spite of these considerations, moment-RT will remain a premiere method for simulating reionization. One of its greatest advantages is that it allows simulations to have a much larger number of resolution elements compared to other RT methods, which has ushered in a new era of coupling RT, hydrodynamics, and galaxy formation.

2.1.2 Ray-tracing

Ray tracing is widely recognized as the most accurate numerical RT method, although the accuracy depends on details of the numerical implementation [59, 63]. It is also the most computationally expensive. These algorithms involve tracing rays around individual sources and calculating the optical depth along each ray, which determines the number of photons absorbed at each location. Rays are attenuated and eventually disappear at large distances from sources when their optical depths reach $\tau \gg 1$.

Three primary types of ray tracing methods have been applied to simulate reionization: long-characteristics, short-characteristics, and adaptive ray tracing (although not all codes fit neatly into these categories). The long-characteristics method traces rays between every cell and every source and integrates along the rays to get the associated optical depths. This is the most expensive method and is mostly intractable for running large reionization simulations for two reasons. First, the number of sources is large (typically \sim millions), and second, radiation travels large distances from the sources after isolated ionized regions overlap, requiring a very large number of rays per source to maintain high spatial resolution. The short-characteristics method reduces computation time by tracing a limited number of rays from the sources in certain directions and then interpolating the column densities of those directly computed cells to obtain the integrated column density between any given source and cell. C²-RAY is a prominent example of a short-characteristics code that has been used extensively for reionization simulations [46, 66].

In adaptive ray tracing, rays split to maintain the level of spatial and angular resolution desired by the user. For a problem with only one source, for instance, only a small number of rays are cast close to the source, and these split as they move further away (increasing angular resolution) to maintain spatial resolution. An adaptive ray tracing method designed for reionization studies was described in Ref. [67], and implemented in several codes [47, 68, 69]. When the radiation from many sources overlaps – as is the case in reionization, particularly near its end – it is often unnecessary to keep track of individual rays from all the sources. In

these instances, rays traveling in approximately the same direction can be merged into a single ray [47]. Ray merging is critical for making the reionization problem more computationally tractable with these schemes.

2.1.3 Monte-Carlo methods

Monte-Carlo methods take a statistical approach to solving the RT equation. They work by sending “photon packets” that travel along random directions drawn from the distribution of angular directions around sources. This method has the advantage that it preserves the full angular dependence of the RT solution (unlike moment-based methods), and it lends itself naturally to problems that involve scattering [e.g. 70, 71]. Indeed, a key feature of the Monte Carlo approach is that, like ray tracing, it converges (in principle) to the exact solution of the RT equation in the limit of an infinite number of photon packets. Moreover, like moment-based methods, the radiation field at each point in space is defined locally, being determined by the local density of photon packets rather than line integrals from distant sources. This locality makes Monte-Carlo codes easier to parallelize efficiently than ray tracing methods, since processors working on different rays will be less likely to have to access the same RT cell simultaneously. However, it also suffers from significant shot noise and poor angular resolution at large distances from isotropic ionizing sources if the number of photon packets is not large enough. Mitigating these issues requires using a large number of photon packets, which increases computational cost. An example of a Monte-Carlo code used for reionization studies is CRASH [72, 73].

2.2 Features of FLEXRT & their motivation

2.2.1 The RT method of choice for FLEXRT

As mentioned earlier, an organizing principle of FLEXRT is flexibility for the user to choose the desired level of accuracy for the problem at hand. Along with this comes the requirement that users should be able to quantify the modeling errors incurred by their choices, e.g. in number of spatial or angular resolution elements. These requirements dictate that the basic RT engine of FLEXRT should be based on the ray tracing and/or Monte Carlo frameworks, as both of these – at least in principle – converge to the exact solution to the RT equation in the limit of an infinite number of rays or photon packets.

The additional need for as much computation speed as possible further narrows the field to either adaptive ray tracing or Monte Carlo RT. Note that adaptive ray tracing allows the user to define the parameters that control how often rays split and merge, making it a naturally flexible method. Monte-Carlo methods share a similar type of flexibility, and have the additional advantage of being easier to parallelize over many CPUs. As we will discuss in detail in §3, the RT method used in FLEXRT is based largely on adaptive ray tracing, with some features that are similar to a Monte-Carlo approach.

2.2.2 Small-scale IGM physics

The multi-scale nature of reionization remains the fundamental challenge of simulating it. Some of the most recent reionization simulations run with moment-based RT have begun to capture the small-scale clumpiness and self-shielding of the intergalactic gas in fully coupled hydro-dynamical boxes with $L \gtrsim 100$ Mpc [e.g. 52, 55]. This unprecedented dynamic range cannot yet be achieved with adaptive ray tracing or Monte Carlo methods, nor in any such moment-based sim that can be run fast enough for parameter space studies. This fact motivates including the effect of small-scale IGM structure into much faster simulations with

coarser resolution in a sub-grid fashion. We address this issue with a key and novel feature available in FLEXRT: its flexible treatment of the ionizing photon opacity. As we describe in §4, the opacity in a cell is treated in a highly generalized way that allows the user to specify an opacity model that accounts for the effects of unresolved IGM physics. This framework can straightforwardly incorporate IGM opacity models based on results from higher resolution radiative hydrodynamics simulations in much smaller volumes. The model introduced in Ref. [21] is one such example. In Ref. [74], we further demonstrated the flexibility of this approach by adding simple prescriptions for possible effects not accounted for in the original model (e.g. additional opacity from massive star-forming halos, recombination radiation, etc.). The freedom to specify the opacity of the IGM flexibly not only gives the user a great deal of control over how the effects of the IGM are modeled; it also provides a way to reduce the computational costs of FLEXRT by orders of magnitude while still modeling the small-scale physics of the ionizing photon sinks.

To summarize, in this section we have briefly outlined the existing numerical approaches for simulating reionization with RT. We have also described some of the key features of FLEXRT and how they serve our goal of developing a flexible code that is useful for situations in between semi-numeric and massive “one-off” RT simulations. The remainder of this paper will describe in detail the core algorithms of FLEXRT and subject them to a battery of validation tests.

3 Adaptive Ray Tracing Implementation

3.1 Ray creation and propagation

In this section, we describe the adaptive ray tracing algorithm employed in FLEXRT. Our algorithm is similar to that described in Ref. [67] and implemented in the RT/hydro code of Ref. [47]. In this method, ray tracing is controlled using HealPix formalism [the Hierarchical Equal Area isoLatitude Pixelation of a sphere, 75]. In each RT cell containing ionizing sources, rays are created at the center of the cell with unit vectors corresponding to the pixels of a HealPix sphere. The number of rays cast is

$$N_{\text{ray}}^{\text{cast}} = 12 \times 4^{l_{\text{hpx}}} \quad (3.1)$$

where $l_{\text{hpx}} \geq 0$ is the integer “level” of the HealPix sphere. Higher levels correspond to spheres with higher angular resolution. Each unit vector is assigned a unique integer HealPix pixel number $0 \leq p < N_{\text{ray}}^{\text{cast}}$ (using the NESTED numbering scheme).

In traditional time-independent ray tracing schemes, rays would be traced away from the source until they either terminate in a neutral region or all their photons are absorbed by the IGM [23, 46, 76]. In FLEXRT, “rays” are treated instead like photon packets that travel a distance Δx_{RT} , the RT cell size, during each time step. Specifically, a ray starting a time step at position (x_0, y_0, z_0) travels to $(x_1, y_1, z_1) = (x_0, y_0, z_0) + \hat{v}\Delta x_{\text{RT}}$ by the end of the time step, where \hat{v} is the unit vector pointing along the original direction of the ray. Photons are absorbed into each cell intersected over this distance following the RT equation (see next section). Each ray retains its original unit vector assigned at casting until it is either split into child rays or merged with other rays (see next sub-sections). This approach, inspired by Monte-Carlo codes, naturally lends itself to the finite speed of light and “localizes” the rays, making FLEXRT easier to parallelize (see §2.1.3). As we will see, this approach makes our procedure for merging of rays particularly straightforward.

To avoid numerical artifacts introduced by the HealPix structure, during each time step we randomly rotate the HealPix spheres used to cast rays around each source by a randomly chosen set of direction angles, α , β , and γ . Each ray retains knowledge of these angles, so that the original HealPix unit vectors associated with it can be recovered when needed. We find that this procedure eliminates discernible structural artifacts even for simulations with just one or very few ionizing sources. Indeed, such artifacts can cause steady-state a-spherical structures in the radiation field around isotropic sources, and so removing them is necessary. An unavoidable side effect of this procedure is that the flux incident on a given cell will “flicker” from one time step to the next as the HealPix directions rotate, averaging to the correct value only over several time steps. This introduces artificial dependence on the ratio of the RT time step and the recombination timescale¹. Fortunately, as we will see, in most relevant applications, either the RT time step is much smaller than the recombination time scale or the local radiation field receives contributions from many sources in a way that averages out this flickering effect. We will comment on this point when it becomes relevant in subsequent sections.

3.2 Ray splitting

Rays can split into “child rays” to maintain a desired level of angular resolution around isolated point sources. A ray of level l_{hpx} is split when it has traveled from its source a distance

$$r_{\text{split}}(l_{\text{hpx}}) = \Delta x_{\text{RT}} 2^{l_{\text{hpx}}} \left(\frac{3}{\pi N_{\text{ray}}^{\text{min}}} \right)^{1/2} \quad (3.2)$$

where $N_{\text{ray}}^{\text{min}}$ is (approximately) the minimum number of rays contained in each cell surrounding the source. This is a free parameter that is set by the user, which can be adjusted to control for the angular resolution of the radiation field and the speed of the computation. Each “parent” ray is split into 4 “child” rays, which have their HealPix parameters updated to

$$l_{\text{hpx}} \rightarrow l_{\text{hpx}} + 1 \quad p \rightarrow 4p + i, i \in [0, 4) \quad (3.3)$$

In the NESTED pixel numbering scheme, these pixels specify four unit vectors that uniformly sub-sample the solid angle corresponding to (l_{hpx}, p) . Figure 2 of Ref. [75] and Figures 1 and 2 of Ref. [67] visualize the sub-division of the HealPix sphere and the splitting procedure used here. Child rays are assigned these new directions and re-positioned to occupy the centers of the new pixels to which they belong. They also retain the same random rotation angles (α , β , and γ) as their parent rays.

3.3 Ray merging

A crucial time (and memory)-saving feature of FLEXRT is that rays traveling in similar directions can merge into a single ray. Ref. [47] demonstrated that ray merging can dramatically speed up ray tracing reionization simulations without substantially sacrificing accuracy. Crucially, as we will see, merging makes it possible to make the scaling of the computation independent of the number of sources (see §2.1.2).

Our implementation of the ray merging is similar to the implementation in the RAD-HYDRO code of Ref. [47] (see §7). We first determine which rays are eligible to be combined

¹Note that *all* Monte Carlo RT (e.g. CRASH, Ref. [72]) codes are subject to this effect at some level, since they randomize the directions of photon packets emitted from sources.

with other rays. All rays are rank-ordered by the number of photons they contain, and the $N_{\text{ex}}N_{\text{RT}}$ rays with the most photons are considered *ineligible* for merging. Here, N_{RT} is the number of RT cells and N_{ex} , the number of rays per cell “exempt” from merging, is a free parameter chosen by the user. As we will see later, excluding the “brightest” rays from the merging procedure helps reduce associated shot noise. All other rays are first grouped by the RT cell they occupy. In each cell, we throw down a randomly oriented HealPix sphere of level l_{merge} (also a user-set parameter) that specifies $12 \times 4^{l_{\text{merge}}}$ independent directions. Finally, rays in the same cell that share the same pixel on that sphere are merged into a single ray traveling in the direction specified by its pixel. Photons are summed over all merged rays, and all other properties (including the ray’s new position) are photon-weighted averages of those of its constituent rays. These ensure that after rays are merged at the end of each time step, the maximum number of rays per cell in the box is

$$N_{\text{ray/cell}}^{\text{max}} = N_{\text{ex}} + 12 \times 4^{l_{\text{merge}}} \equiv N_{\text{ex}} + N_{\text{dir}} \quad (3.4)$$

where $N_{\text{dir}} \equiv 12 \times 4^{l_{\text{merge}}}$ is the number of independent directions used for merging.

Figure 1 shows a 2D representation of the steps in our merging scheme. Panel A shows an RT cell containing a set of rays. The lengths of the rays represent how many photons they contain, and rays with the same colors/line styles point in similar directions. The locations of the bases of the arrows denote the (x, y) positions of the rays. In panel B, we throw down a randomly rotated “pizza” (analogous to a HealPix sphere in 3D) and assign each ray to the slice it occupies. Note that we have consolidated all rays to the center of the panel (ignoring for now their spatial positions) to make it easy to compare their directions. In panel C, rays within the same slice are merged. Note that two of the slices are empty and one of them has only a single ray, so no merging occurs in those slices. In the slice with the red rays, the longest ray had enough photons to be exempt from merging, and the other two were combined. Panel D shows again (x, y) positions of the merged rays, which are the photon-weighted averaged positions of the constituent rays (see again panel A). Note that rays that were not merged with any others (long solid red and dotted black) have not changed their positions.

Figure 2 demonstrates how merging limits the number of rays in a FLEXRT simulation. We show the number of rays per cell vs. number of RT steps for several version of the same $N_{\text{RT}} = 200^3$ FLEXRT simulation with cosmological sources (see §7.2 for details), with several combinations of merging parameters (see legend). The shaded regions denote the interval $[N_{\text{ex}}, N_{\text{ex}} + N_{\text{dir}}]$. For $N_{\text{ray}}/N_{\text{RT}} < N_{\text{ex}}$, all rays are exempt from merging, and the number of rays grows with time as a steep power law. Upon reaching N_{ex} , $N_{\text{ray}}/N_{\text{cell}}$ stalls as merging begins restricting the number of rays in ionized cells. The ray count increases gradually thereafter, plateauing slightly below $N_{\text{ray/cell}}^{\text{max}}$ (Eq. 3.4) once the entire volume ionizes. By adjusting l_{hpx} and N_{ex} , the user can control the number of rays in the simulation (determining its computational cost), and the angular/spatial resolution of the radiation field.

4 Treatments of the IGM Opacity

As stated in §1 and 2.2.2, FLEXRT’s other key feature is its flexible treatment of the opacity of the ionized IGM. In fact, FLEXRT has two “modes” for doing this, between which the user can choose. The first, which we will refer to as the “Standard Mode” and will describe in §4.1, solves directly for the chemistry of the gas and its opacity using a method very similar to that employed in the C2-Ray code of Ref. [46]. The other approach, described in §4.2, uses a

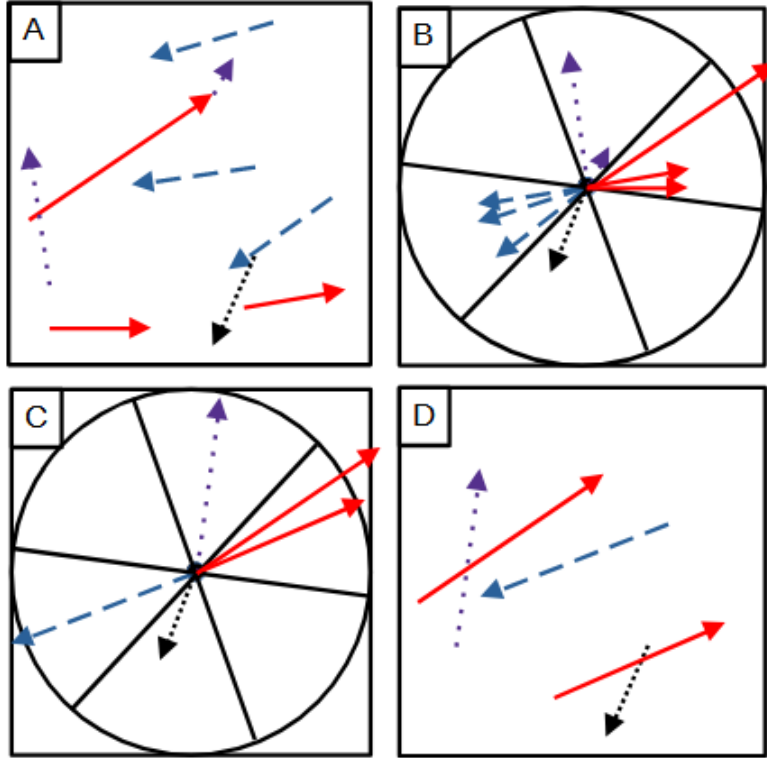


Figure 1. 2D representation of how ray merging works in FLEXRT. Panel A shows a cell containing several rays. The lengths of the arrows represent the number of photons in each ray, and rays with same color/line style point in similar directions. The location of the bases of the arrows denotes the (x, y) positions of the rays. In panel B, we throw down a randomly rotated “pizza” (analogous to a HealPix sphere in 3D) and group rays by the “slice” that they occupy, placing their bases in the center of the panel to aid comparison of their directions. We merge rays occupying the same slice in panel C, excluding the longest (red) ray, since it has enough photons to be exempt. Merged rays point along the bisector of the slice they occupy (i.e. the HealPix pixel direction). In panel D, we show that the positions of merged rays are the photon-weighted average of their constituents.

highly general treatment for the IGM opacity that relies on flexible external input. We refer to this as “Generalized Opacity Mode”.

4.1 Direct solution of the chemistry equations (“Standard Mode”)

In this mode, we assume that all small-scale fluctuations in the HI number density (n_{HI}) are fully resolved by our simulation. That is, n_{HI} does not fluctuate below the scale of the RT cell, Δx_{RT} . Under this assumption, we can write an initial guess for the HI photo-ionization rate Γ_{HI} at the beginning of an RT time step of length $\Delta t = \Delta x_{\text{RT}}/c$ as:

$$\Gamma_{\text{HI}}^{i,0} = \sum_{j=1}^{N_{\text{rays}}} \sum_{\nu=1}^{N_{\text{freq}}} \frac{N_{\gamma}^{ij\nu} (1 - \exp[-n_{\text{HI}}^{i,0} \sigma_{\text{HI}}^{\nu} \Delta s_{ij}]/\Delta t)}{V_{\text{cell}}^i n_{\text{HI}}^{i,0}} \quad (4.1)$$

Here, Δs_{ij} the path length of ray j through i during Δt . $N_{\gamma}^{ij\nu}$ is the number of photons initially in frequency bin ν of ray j , and the sum runs over all rays that intersect cell i during Δt . The initial HI number density in cell i is $n_{\text{HI}}^{i,0}$, V_{cell}^i is the cell volume, and σ_{HI}^{ν} is the

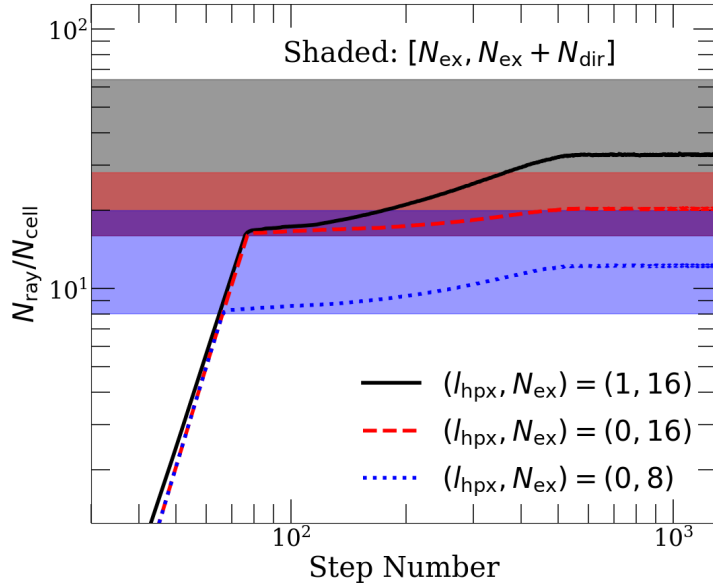


Figure 2. Examples of how merging limits the number of rays in FLEXRT simulations. The curves show the number of rays per cell vs. number of RT steps for a simulation with $N_{\text{cell}} = 200^3$, and several values of l_{hpX} and N_{ex} (see legend). The shaded region the range between N_{ex} and $N_{\text{ex}} + N_{\text{dir}}$, where $N_{\text{dir}} = 12 \times 4^{l_{\text{hpX}}}$ is the number of independent directions allowed in the HealPix merging scheme. The number of rays per cell grows like a power law with the number of step until reaching N_{ex} , after which it grows much more slowly. The number of rays (after the merging step completes) can never exceed $N_{\text{ray/cell}}^{\text{max}} = N_{\text{ex}} + N_{\text{dir}}$, and may be somewhat less than that, since most cells do not contain rays pointing in every allowed direction. In all cases, $N_{\text{ray}}/N_{\text{cell}}$ plateaus slightly below $N_{\text{ray/cell}}^{\text{max}}$ once all cells in the volume are ionized.

ionization cross-section of HI in frequency bin ν . The numerator is the number of ionizations in cell i and the denominator is the initial *number* of HI atoms.

The ionization balance equation for HI is

$$\frac{dn_{\text{HI}}}{dt} = -(\Gamma_{\text{HI}}n_{\text{HI}} + C_{\text{HI}}(T)n_e) + \alpha(T)n_en_{\text{HII}} \quad (4.2)$$

where T is temperature, $C_{\text{HI}}(T)$ is the collisional ionization coefficient of HI, $\alpha(T)$ is the recombination coefficient of HII, n_e is the electron number density and n_{HII} is the HII number density. Updating Eq. 4.2 using Eq. 4.1 would ignore the fact that n_{HI} and Γ_{HI} may evolve during Δt . Following Ref. [46], we account for this by solving for the time-dependence of the ionized fraction x_i during Δt assuming that the recombination rate remains constant (Eq. 12-14 of Ref. [46]),

$$x_i(t) = x_{\text{eq}} + (x_0 - x_{\text{eq}})e^{-t/t_i} \quad (4.3)$$

where x_0 is the ionized fraction at the beginning of the time step, and

$$x_{\text{eq}} = \frac{\Gamma_{\text{HI}} + C_{\text{HI}}(T)n_e}{\Gamma_{\text{HI}} + C_{\text{HI}}(T)n_e + \alpha(T)n_e} \quad (4.4)$$

$$t_i = \frac{1}{\Gamma_{\text{HI}} + C_{\text{HI}}(T)n_e + \alpha(T)n_e} \quad (4.5)$$

Then the time-averaged ionized fraction during the time step is

$$\langle x_i \rangle = x_{\text{eq}} + (x_0 - x_{\text{eq}})(1 - e^{-\Delta t/t_i}) \frac{t_i}{\Delta t} \quad (4.6)$$

From this we can calculate the time-averaged average HI number density, $\langle n_{\text{HI}} \rangle$, and recalculate Γ_{HI} :

$$\Gamma_{\text{HI}}^i = \sum_{\nu=1}^{N_{\text{freq}}} \sum_{j=1}^{N_{\text{rays}}} \frac{N_{\gamma}^{ij\nu} (1 - \exp[-\langle n_{\text{HI}}^i \rangle \sigma_{\text{HI}}^{\nu} \Delta s_{ij}] / \Delta t)}{V_{\text{cell}}^i \langle n_{\text{HI}}^i \rangle} \quad (4.7)$$

We iterate Eq. 4.3-4.7 several times to achieve convergence. Ref. [46] pointed out that this procedure gives the exact solution for n_{HI} , no matter how large Δt is, if recombinations are neglected. Generally, n_{HI} evolves most quickly inside ionization fronts, which are generally very thin (10s of ckpc [77]) and move very fast ($10^3 - 10^4$ km/s), such that the integrated number of recombinations taking place *inside* I-fronts is small compared to the number in ionized gas elsewhere. Thus, in the situations where the iteration procedure described above is most important, it is generally a good approximation to neglect recombinations. Note that the “inside” of the I-front refers to gas within the thin boundary between highly ionized ($x_{\text{HI}} \sim 0$) and fully neutral ($x_{\text{HI}} \sim 1$) gas.

However, one problem with Eq. 4.7 is that if Δx_{RT} is much larger than the I-front width Δx_{IF} , the I-front will be “smeared out” uniformly over the cell containing it. This is because n_{HI} is assumed to have a uniform value everywhere in the cell. A more accurate treatment would divide the cell into a highly ionized and fully neutral component, and track the fraction of the cell in each state as the I-front crosses it. As we will see in the next sub-section, this is precisely the approach used in the Generalized Opacity Mode of FLEXRT. In Standard Mode, the error resulting from this smearing effect is that the recombination rate in partially ionized cells is too low by approximately a factor of $\langle x_i \rangle$ whenever $\Delta x_{\text{RT}} \gg \Delta x_{\text{IF}}$. As such, Standard Mode can under-estimate the integrated recombination rate if Δx_{RT} is large enough - we will return to this point in §6.

The temperature in each cell is given by the solution of Ref. [78],

$$\frac{dT}{dt} = \frac{2}{3k_{\text{B}}n_{\text{tot}}} (\mathcal{H} - \Lambda) - 2H(z)T - \frac{T}{n_{\text{tot}}} \frac{dn_{\text{tot}}}{dt} + \frac{2T}{3\Delta} \frac{d\Delta}{dt} \quad (4.8)$$

In the first term on the RHS, \mathcal{H} and Λ , are the net radiative heating and cooling rates, respectively, n_{tot} is the total number density of gas particles (neutrals, ions, and electrons), and k_{B} is Boltzmann’s constant. We include heating by photo-ionizations as well as cooling by recombinations, collisional ionizations and excitations, free-free interactions, and Compton scattering off the CMB. The second term, wherein $H(z)$ is the Hubble parameter, accounts for adiabatic cooling by cosmic expansion. The third term accounts for changes in temperature from an increase or decrease in the number of particles in the gas. The last term accounts for heating/cooling by compression/expansion, and is proportional to the change in the density in units of the mean, Δ .

4.2 General treatment (“Generalized Opacity Mode”)

FLEXRT’s second mode is built around relaxing the assumption that small-scale fluctuations in n_{HI} are fully resolved. Relaxing this assumption allows for each cell to have some unresolved spatial distribution of n_{HI} inside it that would not be accounted for in Standard Mode. In this case, the equations in the previous section become ill-defined, since they rely

on assuming a single value for n_{HI} in each cell. A commonly-employed method to correct for the effect of un-resolved density fluctuations is to boost the recombination rate (and thus, the residual n_{HI} in photo-ionization equilibrium) in each cell by a sub-grid clumping factor [e.g. 38]. However, this is not the most general approach, since it assumes that the ionizing opacity is determined uniquely by the recombination rate (e.g. Eq. 17 of Ref. [79]). This is not true in the presence of dense, self-shielding structures that harbor neutral gas, wherein the assumption of photo-ionization equilibrium may not hold. Specifically, neutral gas embedded in dense clumps may be in the process of photo-evaporation, or low-density ionized gas may be accreting onto denser structures and rapidly recombining. In these scenarios, the ionization rate can be larger or smaller than the recombination rate, respectively.

A more general approach is to forgo trying to model n_{HI} entirely, and instead focus on the effective frequency-dependent absorption coefficient κ_ν associated with each cell. The opacity to ionizing photons across a path length Δs through the cell is given by

$$\tau_\nu \equiv \kappa_\nu \Delta s \equiv \Delta x_{\text{RT}} / \lambda_\nu \quad (4.9)$$

where we have defined $\lambda_\nu \equiv 1/\kappa_\nu$ to be the effective mean free path (note that we will use both κ_ν and λ_ν in what follows). Here, κ_ν is defined to be the mean “effective” absorption coefficient in the cell. This means that κ_ν is defined such that on average, Eq. 4.9 returns the correct opacity for any length Δs along any direction. In §4.1, where we assumed a uniform n_{HI} in each cell, $\kappa_\nu = n_{\text{HI}}\sigma_{\text{HI}}^\nu$ and $\tau_\nu = n_{\text{HI}}\sigma_{\text{HI}}^\nu\Delta s$. Another example is the sub-grid model described in Refs. [21, 35]. There, λ_ν is calculated from a suite of high-resolution, small-volume simulations using a definition that satisfies these conditions (see Appendix C of Ref. [35] for a derivation).

We begin by making an initial guess for Γ_{HI} that does not require knowledge of either n_{HI} or κ_ν . We can get this by taking the limit of Eq. 4.1 for $\tau_\nu \ll 1$, which simplifies to

$$\Gamma_{\text{HI}}^{i,0} = \sum_{\nu=1}^{N_\nu} \sum_{j=1}^{N_{\text{rays}}} \frac{N_\gamma^{ij\nu} \sigma_{\text{HI}}^\nu \Delta s_{ij}}{V_{\text{cell}}^i \Delta t} = \sum_{\nu=1}^{N_\nu} F_\gamma^{i,\nu} \sigma_{\text{HI}}^\nu \quad (4.10)$$

where $F_\gamma^{i,\nu}$ is the photon number flux in frequency bin ν incident on cell i ². Eq. 4.10 is crucial because, as we will see, *any* reasonable procedure for determining λ_ν requires first having at least a guess for Γ_{HI} .

The next step is to determine κ_ν . A highly general functional form for κ_ν at some redshift z is given by

$$\kappa_\nu(z) = G_\kappa(z, t, \Delta(z, t), \Gamma_{\text{HI}}(z, t), x_i(z, t), T(z, t), \nu) \quad (4.11)$$

Here, Δ , Γ_{HI} , x_i , and T are the density in units of the mean, photo-ionization rate, ionized fraction, and temperature of a given cell, respectively. We use z to refer to the current time, while t indicates the history of a quantity prior to z . The statement here is that κ_ν can, in general, be some function not only of the current physical conditions in a cell, but also of the prior history of those conditions. One example, encapsulated in $x_i(z, t)$, is the dependence of κ_ν on the prior reionization history. Indeed, several studies (e.g. Refs. [80–82]) have found that the opacity of the IGM in some region depends not only on the current redshift, but also on when that region was reionized.

²To get the second equality, we have used the fact that $\sum_{j=1}^{N_{\text{rays}}} \frac{N_\gamma^{ij\nu} \Delta s_{ij}}{V_{\text{cell}}^i \Delta t}$ is the total incident ionizing photon number flux in frequency bin ν .

Before continuing, it is worth emphasizing that the approach described in this section is so versatile because Eq. 4.11 can have practically any form imaginable, and the equations given below will still hold. Ref. [21] provides but one example. There, G_κ takes the form of a sub-grid model for the ionizing opacity calibrated to the results of high-resolution radiative hydrodynamics simulations. In Ref. [74], we explored adding other contributions to κ_ν , highlighting the flexibility of our framework (see §3.6 and Appendix D of that work).

Our final task is to provide a general expression for Γ_{HI} given knowledge of κ_ν . Indeed, if Δx_{RT} were assumed to always be $\ll \lambda_\nu$, Eq. 4.10 would be sufficient. However, as already mentioned, a key feature of FLEXRT is that it should admit the use of large (up to several Mpc) RT cells without substantial loss of accuracy. As such, we must allow for scenarios in which $\lambda_\nu \lesssim \Delta x_{\text{RT}}$. We can do this as follows. First, we assume (without loss of generality, as we will see) that all rays j during the time step Δt are incident on one face of cell i traveling in the direction normal to that face. We can write the contribution of ray j to Γ_{HI} at a distance x_j into the cell as

$$\begin{aligned} \Gamma_{\text{HI}}^{ij}(x_j) &= \sum_{\nu=1}^{N_\nu} F_\gamma^{ij\nu} \exp(-x_j/\lambda_\nu) \sigma_{\text{HI}}^\nu = \\ &= \sum_{\nu=1}^{N_\nu} \frac{N_\gamma^{ij\nu}}{A_{\text{cell}}^i \Delta t} \exp(-x_j/\lambda_\nu) \sigma_{\text{HI}}^\nu \end{aligned} \quad (4.12)$$

where $A_{\text{cell}} \equiv \Delta x_{\text{RT}}^2$ and we have averaged the incident ionizing flux across the transverse directions. The first expression follows from λ_ν being constant across the cell by definition.³ Next, we average Γ_{HI}^{ij} in the incident direction across the length of the cell, Δx_{RT} , and sum over all rays. The path length traversed by the ray is Δs_{ij} , which is always $\leq \Delta x_{\text{RT}}$ (as enforced by our choice of time step, $\Delta t = \Delta x_{\text{RT}}/c$). This gives

$$\begin{aligned} \langle \Gamma_{\text{HI}} \rangle^i &= \sum_{j=1}^{N_{\text{rays}}} \sum_{\nu=1}^{N_\nu} \frac{1}{\Delta x_{\text{RT}}} \int_0^{\Delta s_{ij}} dx_j \frac{N_\gamma^{ij\nu}}{A_{\text{cell}}^i \Delta t} \exp(-x_j/\lambda_\nu) \sigma_{\text{HI}}^\nu \\ &= \sum_{j=1}^{N_{\text{rays}}} \sum_{\nu=1}^{N_{\text{freq}}} \frac{N_\gamma^{ij\nu} [1 - \exp(-\Delta s_{ij}/\lambda_\nu^i)] \sigma_{\text{HI}}^\nu \lambda_\nu^i}{V_{\text{cell}}^i \Delta t} \end{aligned} \quad (4.13)$$

In the second equality, we have evaluated the integral and used the fact that $A_{\text{cell}} \Delta x_{\text{RT}} = V_{\text{cell}}$. Importantly, we see that Eq. 4.13 simplifies to Eq. 4.7 in the limit that $\lambda_\nu = 1/[\sigma_{\text{HI}}^\nu n_{\text{HI}}]$, which is the case in Standard mode. This demonstrates that Eq. 4.13 does not depend on the plane-parallel geometry assumed in its derivation. Eq. 4.11 and 4.13 are updated iteratively until a self-consistent solution for λ and Γ_{HI} is reached.

We note that the components of Eq. 4.13 have straightforward interpretations. First of all, $N_\gamma^{ij\nu} [1 - \exp(-\Delta s_{ij}/\lambda_\nu^i)] / \Delta t$ is simply the number of photons absorbed into cell i from ray j per unit time, and the sum of this over rays is the total ionization rate. Since Γ_{HI} is defined to be the number of ionizations per unit time divided by the number of neutral atoms, then

³The astute reader may wonder if this assumption contradicts our earlier observation that n_{HI} is not constant within cells. It does not because the isotropically-averaged opacity over some in-homogeneous region of the IGM still captures the average effect of the density fluctuations. The assumption here is that all information about the un-resolved in-homogeneity in n_{HI} is encoded in λ_ν (via whatever function is used for Eq. 4.11).

the remaining factor of $V_{\text{cell}}/[\sigma_{\text{HI}}^{\nu}\lambda_{\nu}]$ can be interpreted as the number of neutral atoms subject to ionization by radiation in the cell (excluding any self-shielded systems, where Γ_{HI} would locally be 0 and no atoms can be ionized). Indeed, this is trivially the case if n_{HI} is assumed uniform, since $\lambda_{\nu} = 1/\kappa_{\nu} = 1/n_{\text{HI}}\sigma_{\text{HI}}^{\nu}$. We showed in Appendix B of Ref. [35] that for the sub-grid opacity model used in that work, $\langle\lambda\rangle_{\nu} = 1/n_{\text{HI}}^{\Gamma}\langle\sigma_{\text{HI}}\rangle_{\nu}$ to a good approximation, where n_{HI}^{Γ} is the Γ_{HI} -weighted average neutral hydrogen density and $\langle\dots\rangle_{\nu}$ denotes an appropriately defined average over frequency. For the specific definition of λ_{ν} adopted in Ref. [74], Eq. 4.13 is equivalent to their Eq. 7, although Eq. 4.13 is more general.

Eq. 4.10-4.13 apply to highly ionized regions. To track the growth of these regions, we assume that the boundary between highly ionized and fully neutral gas (that is, the I-front) is infinitely thin - this is the so-called “moving screen” approximation⁴. This is equivalent to assuming that $\Delta x_{\text{IF}} \ll \Delta x_{\text{RT}}$. Indeed, it is the opposite assumption to that made in the §4.1, namely that n_{HI} is uniform within partially ionized cells. Given our earlier discussion of the intended application of FLEXRT’s Generalized Opacity formalism, it is reasonable to expect that this condition should hold in most relevant contexts (that is, when RT cells are \sim a few Mpc). In subsequent sections, we will highlight this assumption whenever it becomes relevant (as it will in several instances). We will also explicitly demonstrate the regime in which this approximation is valid in §6. The evolution of the ionized fraction x_{ion} in a cell is (in the non-relativistic limit)

$$\frac{dx_{\text{ion}}}{dt} = \frac{v_{\text{IF}}}{\Delta x_{\text{RT}}} = \frac{F_{\gamma}}{(1 + \chi)n_{\text{H}}\Delta x_{\text{RT}}} \quad (4.14)$$

where v_{IF} is the I-front speed, F_{γ} is the ionizing flux incident on the neutral component of the cell, n_{H} is the hydrogen number density, and the factor of $1 + \chi$ accounts for single ionization of helium along with hydrogen⁵. For partially ionized cells, we evaluate Γ_{HI} (Eq. 4.13) for the ionized component by making the substitutions

$$\Delta s_{ij} \rightarrow x_{\text{ion}}\Delta s_{ij} \quad V_{\text{cell}}^i \rightarrow x_{\text{ion}}V_{\text{cell}}^i \quad (4.15)$$

Note that photons contribute to F_{γ} in Eq. 4.14 only after they have traveled a distance $x_{\text{ion}}\Delta s_{ij}$ through a cell. This condition assumes that rays enter partially ionized cells on the “ionized side” of the cell, which is not always the case. However, this geometry is physically reasonable since rays will generally move in the same direction as the I-front.

The peak gas temperature immediately behind an I-front, T_{reion} , is set by the heating and radiative cooling inside of the I-front [83, 84]. Generalized Opacity Mode is designed for large-volume simulations of reionization that do not resolve the small distance scales and short timescales necessary to capture this physics. Hence, in this mode, T_{reion} is a user-specified parameter, for which our default model is that of Ref. [83]. They demonstrated that T_{reion} depends mainly on the velocity of the I-front and the spectral index of the flux driving it - with the former being the dominant effect as long as the spectrum is not very soft or the I-front very fast. For all simulations presented in this paper, T_{reion} is obtained from the fitting function of Ref. [83], which assumes $\alpha = 1.5$.⁶ We note, however, that any model for T_{reion} can

⁴Note that a similar assumption is used in the RADHYDRO code.

⁵We note that x_i in Eq. 4.14 is defined as the fraction of a given cell that is in a highly ionized (vs. fully neutral) state, which is not quite the same as the ionized fraction of the cell. This is because highly ionized gas still retains a small fraction of neutral gas that is not included in the definition of this quantity.

⁶Their fitting function requires I-front speeds as input, which we compute using the flux-based method also described in Ref. [83].

be implemented into the code. For example, one may choose to implement the more general model provided by the interpolation tables of Ref. [83], which include the dependence on α . We track the subsequent thermal evolution of the gas in Generalized Opacity mode using Eq. 4.8. However, since we do not know n_{HI} , we cannot directly compute the photo-heating rate or the collisional cooling rates (ionization and excitation). To estimate the photo-heating rate, we assume that the number of ionizations in ionized gas is balanced by the number of recombinations (that is, photo-ionization equilibrium). Assuming the ionizing radiation has a power law spectrum with index α and a cutoff at 4 Ryd, the heating rate due to HI ionizations is given by

$$\mathcal{H}_{\text{HI}} = E_{\text{HI}} \left(\frac{\alpha + \beta}{\alpha + \beta - 1} \frac{1 - 4^{1-\beta-\alpha}}{1 - 4^{-\beta-\alpha}} - 1 \right) \alpha_{\text{A}}(T) n_e n_{\text{HI}} \quad (4.16)$$

where $\beta = 2.75$ is the approximate power-law scaling of σ_{HI} with ν and $E_{\text{HI}} = 1$ Ryd is the ionization energy of HI. We include an analogous expression to account for heating due to HeI ionizations. The collisional cooling rates can be estimated using a similar approximation.

5 Cosmological RT Comparison Project (2006) Tests

In this section, we will subject FLEXRT to the four static density tests introduced in the Cosmological Radiative Transfer Comparison Project⁷ (CRTCP) [59, henceforth I06]. We will perform each test in both Standard and Generalized Opacity mode, and compare them to each other and results from the CRTCP.

5.1 Iso-thermal Stromgren Sphere (Test #1)

The first test in I06 is perhaps the simplest cosmologically relevant RT problem - the growth of an HII region around an isotropic point source in a homogeneous, isothermal region. This is one of the only RT problems with a closed-form analytic solution. Assuming the source produces \dot{N}_γ ionizing photons per unit time, and that the boundary between ionized and neutral gas is infinitely thin, the radius and velocity of the I-front are given by (Eq. 5-7 of I06),

$$r(t) = r_S (1 - \exp[-t/t_{\text{rec}}])^{1/3} \quad (5.1)$$

$$v(t) = \frac{r_S}{3t_{\text{rec}}} \frac{\exp[-t/t_{\text{rec}}]}{(1 - \exp[-t/t_{\text{rec}}])^{2/3}} \quad (5.2)$$

where the Stromgren radius is given by

$$r_S \equiv \left(\frac{3\dot{N}_\gamma}{4\pi\alpha_{\text{B}}(T)n_{\text{H}}} \right)^{1/3} \quad (5.3)$$

is the $t \rightarrow \infty$ limit of $r(t)$. Here, α_{B} is the case B recombination rate of the gas, T is the temperature, and n_{H} is the hydrogen number density. The recombination timescale is

$$t_{\text{rec}} \equiv \frac{1}{\alpha_{\text{B}}(T)n_{\text{H}}} \quad (5.4)$$

Following I06, we assume $n_{\text{H}} = 10^{-3} \text{ cm}^{-3}$, $T = 10^4 \text{ K}$, and $\dot{N}_\gamma = 5 \times 10^{48} \text{ photons/s}$, and a photon energy of 13.6eV (the ionization energy of hydrogen). Our computation volume

⁷https://astronomy.sussex.ac.uk/~iti20/RT_comparison_project/index.html

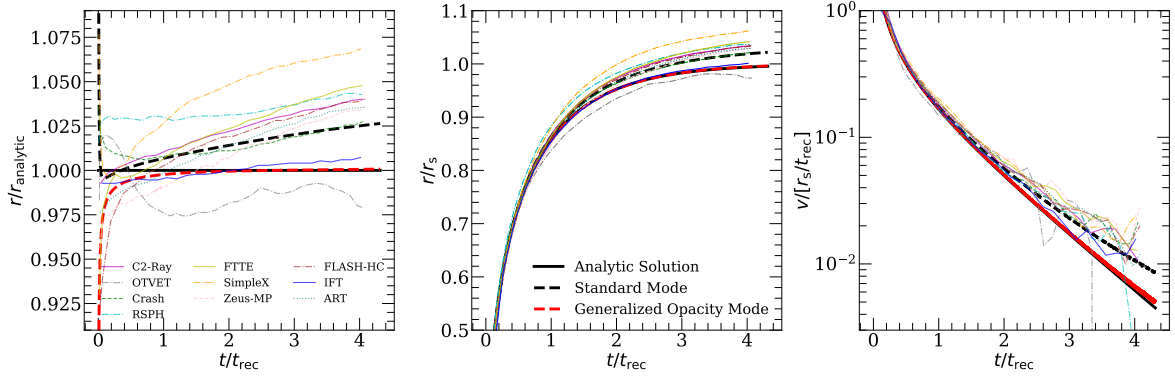


Figure 3. Growth of an isothermal, spherically symmetric HII region around a single source. The left and middle panels show the ratio of the simulated $r(t)$ with the analytic solution (Eq. 5.1) and the Stromgren radius (Eq. 5.3), respectively, vs. time in units of t_{rec} (Eq. 5.4). The right panel shows the I-front velocity in units of r_S/t_{rec} . The black and red dashed curves show results for Standard and Generalized Opacity mode, respectively, while the solid black line denotes the analytic solution. The other curves denote results from codes presented in I06 [46, 62, 72, 85–91]. Both modes of FLEXRT agree well with the analytic prediction. Generalized Opacity mode yields sub-percent agreement since, like the analytic model, it assumes an infinitely sharp I-front. Like most CRTCP codes, Standard mode predicts a slightly larger HII radius than the analytic prediction, owing to the finite width of the I-front.

is a box with $L = 13.2$ pkpc with the source at the center⁸. We use $N = 100^3$ RT cells and a reduced speed of light of $\tilde{c} = 0.01$. The reduced speed of light is appropriate here because the I-front speed, v_{IF} , is much less than \tilde{c} except at the beginning of the test.

As discussed previously, in Generalized Opacity mode we do not (a-priori) specify a prescription for λ_ν (Eq. 4.11). We must therefore do so here before proceeding with this and subsequent tests. Assuming no unresolved density fluctuations (which is trivially the case here), we can write for each cell (see §4.1),

$$\lambda_\nu = \frac{1}{\sigma_{\text{HI}}^\nu n_{\text{HI}}} \quad (5.5)$$

For highly ionized gas, we can assume photo-ionization equilibrium,

$$\Gamma_{\text{HI}} n_{\text{HI}} = \alpha(T) n_e n_{\text{HII}} \quad (5.6)$$

which can be solved for n_{HI} to give

$$n_{\text{HI}} = \frac{\alpha(T) n_e n_{\text{HII}}}{\Gamma_{\text{HI}}} \approx \frac{\alpha(T) n_{\text{H}}^2}{\Gamma_{\text{HI}}} \quad (5.7)$$

The last equality is motivated by our moving-screen I-front prescription (Eq. 4.14), which assumes that $n_{\text{HI}} \ll n_{\text{H}}$ behind the I-front. We will use Eq. 5.5 and 5.7 to solve for λ_ν and estimate n_{HI} in Generalized Opacity mode in all the tests that follow in this section. Note that this prescription is just one very special case of Eq. 4.11.

Figure 3 shows the evolution of the I-front position and velocity for Test #1. The left panel shows the ratio of the isotropically-averaged I-front radius with the analytic prediction

⁸As noted by I06, $r_S = 5.4$ pkpc for this test, motivating this box size.

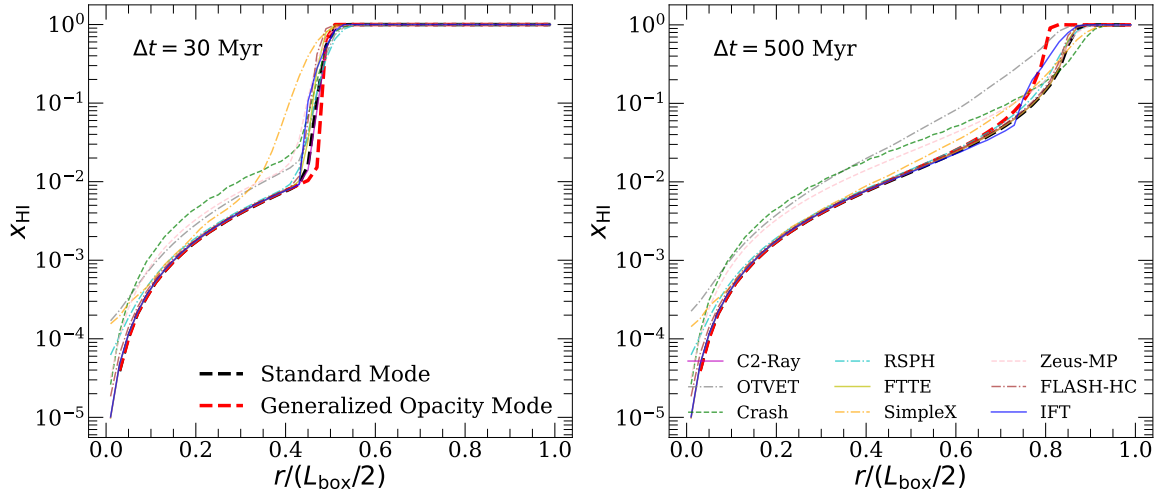


Figure 4. Spherically averaged HI fraction profile for Test #1 at $\Delta t = 30$ Myr (left) and 500 Myr (right). The two modes agree closely for gas behind the I-front. The gas transitions to neutral more abruptly at $\Delta t = 500$ Myr in Generalized Opacity mode, owing to the assumption of sharp I-fronts. The profiles are also in good agreement with CRTCP codes. Standard mode closely matches C2-Ray, as expected since the ionization solvers in those codes are very similar.

(Eq. 5.1), while the middle and right panels show the evolution of $r(t)$ and $v(t)$. Following I06, we express distance and time in units of r_s and t_{rec} , respectively. The black and red dashed curves show results for Standard and Generalized Opacity mode, respectively, while the black solid curve shows the analytic result. The other thin curves are all results from CRTCP codes. In Standard mode, the HII region expands slightly faster than the analytic solution and reaches a slightly larger volume. Indeed, most of the CRTCP codes do this, reaching final radii a few percent larger than r_s . This is in part because the I-front is not infinitely sharp⁹, as the analytic solution assumes. Generalized Opacity mode agrees with the analytic prediction within $\ll 1\%$ at $t > 2t_{\text{rec}}$. This is because it treats the I-front as infinitely sharp, matching the assumption of the analytic solution. We also note that Generalized Opacity mode is very close to the result of from I-Front Tracker (IFT), which makes the same assumption.

Figure 4 shows the angle-averaged HI fraction (x_{HI}) profile as a function of distance from the source. The left and right panels show results at $\Delta t = 30$ and 500 Myr, respectively. Note that in Generalized Opacity mode, the HI fraction is not calculated explicitly, and so we must invert Eq. 5.5 to get it. The two modes agree well with each other at $t = 30$ Myr, when the I-front is sharpest. At $t = 500$ Myr, when the I-front has nearly stopped, a larger difference emerges. The transition from highly ionized to neutral is wider in Standard mode and extends to a larger distance from the source. Behind the I-front, the profile of residual HI is in good agreement. Standard mode is in tight agreement with several CRTCP modes, particularly C2-Ray. This makes sense because standard mode and C2-Ray have very similar ionization solvers. Once again, Generalized Opacity mode agrees best with IFT.

Figure 5 shows slices of the HI fraction through the center of the box at $t = 30$ and 500 Myr (top and bottom rows, respectively)¹⁰. In the 1st and 2nd column, we compare Standard mode to C2-Ray, since these use similar methods to solve for the ionization state

⁹And perhaps also due to the an-isotropic nature of the Cartesian mesh.

¹⁰We only show one corner of the HII region, since the CRTCP tests do not simulate the entire sphere.

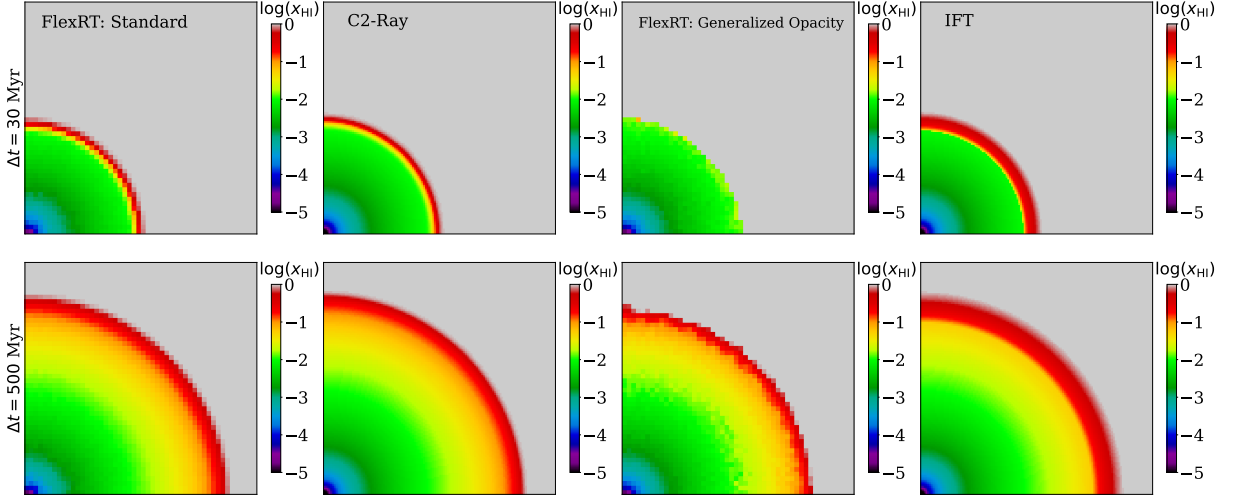


Figure 5. Visualization of Test #1 - expansion of an isothermal, spherically symmetric HII region around a point source. We show quarter-slices of $\log(x_{\text{HI}})$ through the center of the HII region at $\Delta t = 30$ Myr (top row) and 500 Myr (bottom row). From left to right, the columns show results for Standard mode, C2-Ray (from I06), Generalized Opacity mode, and IFT (from I06). Standard and C2-Ray are in excellent visual agreement. In Generalized Opacity mode, the boundary between highly ionized and neutral gas is much sharper at $\Delta t = 30$ Myr, owing to its sharp I-front treatment. In IFT, there is a similarly sharp jump from highly ionized gas (with $x_{\text{HI}} < 0.01$) to significantly neutral gas (with $x_{\text{HI}} > 0.1$). However, IFT has an extended region with $x_{\text{HI}} < 1$ in front of this jump, while in Generalized Opacity mode x_{HI} goes straight to unity. Generalized Opacity mode also displays a noisier x_{HI} field, since x_{HI} is estimated in each cell based on its instantaneous value of Γ_{HI} , and is more sensitive to ray-tracing related artifacts in the radiation field than the time-integrated x_{HI} in Standard mode.

of the gas. The 3rd and 4th columns compare Generalized Opacity mode to IFT, since these both assume sharp boundaries between ionized and neutral gas. We find excellent visual agreement between FLEXRT and C2-Ray at both times. Generalized Opacity mode displays a much sharper boundary between ionized and neutral gas, especially at $\Delta t = 30$ Myr, reflecting its sharp I-front treatment. In IFT, there is a similarly sharp jump between highly ionized ($x_{\text{HI}} < 0.01$) gas and highly neutral gas, although x_{HI} does not jump immediately to unity as it does in Generalized Opacity mode. There is also some noise noticeable in Generalized Opacity mode, particularly at $\Delta t = 500$ Myr. This is a manifestation of the “flickering” effect arising from rotating the HealPix unit vectors associated with the source on each time step. The reason these are visible in Generalized Opacity Mode and not Standard Mode is because, in the former, λ is calculated using the instantaneous value of Γ_{HI} (Eq. 5.5-Eq. 5.7), such that the neutral fraction effectively reacts instantaneously to changes in incident flux. Note that this is not the case in the sub-grid model described in Refs. [21, 35], which includes some dependence of λ on the prior history of Γ_{HI} . In Standard Mode, n_{HI} is the result of time integration (Eq. 4.6), and is thus much less sensitive to this effect. Fortunately, the tight agreement of Generalized Opacity Mode with the analytic expectation in Figure 3 suggests that this does not significantly affect the recombination rate in this test.

This test validates the most basic functions of the code - the ray transport and splitting (§3.2) algorithms, and the two opacity solvers (§4). Since this is a test with only one source, we do not use the merging algorithm (§3.3), which is expected to work well only in the limit

of many sources (tests of the merging algorithm are presented in §7.) It also highlights some of the key similarities and differences between the Standard and Generalized Opacity modes, including how they handle I-fronts and how sensitive they are to ray-tracing artifacts in the radiation field.

5.2 Stromgren sphere with T evolution (Test #2)

Our next test has the same setup as #1, but with evolving gas temperature. Following I06, we set the initial gas temperature to 100 K and use a blackbody spectrum with temperature $T_{\text{bb}} = 10^5 \text{K}$ for the source. For this and subsequent tests, we have included collisional cooling processes in Generalized Opacity mode by using Eq. 5.7 to get n_{HI} , then calculating the rates using cooling coefficients from Ref. [78]. Figure 6 shows the growth of the HII region in the same format as Figure 3. Note that for consistency with I06, we continue to show the constant-temperature analytic solution from Figure 3 as a reference, even though it does not describe the evolving temperature case accurately. The I-front grows slightly faster than it did in Test #1, finishing with a radius $\approx 12\%$ (4%) larger than the analytic prediction for Standard (Generalized Opacity) mode. This is because the temperature in the ionized region is higher than 10^4K , which reduces the recombination rate and increases r_S (Eq. 5.3) relative to Test #1.

Both modes of FLEXRT agree broadly with the CRTCP codes. One notable difference is that Standard mode produces a slightly larger Stromgren sphere than all the CRTCP codes. This could be in part due to differences in the amount of pre-heating ahead of the I-front, which changes the recombination rate near the edge of the ionized region. This effect is determined by the frequency resolution of the ionizing spectrum and the assumed physics of pre-heating, which differ considerably between the CRTCP codes (as pointed out by I06). Another factor could be that our estimate of r is based on the total ionized fraction in the box, assuming a sharp boundary between ionized and neutral gas. Since the I-front in standard mode is asymmetric in the radial direction, this definition may slightly over-estimate the true I-front location. Generalized Opacity mode agrees reasonably well with IFT, but has a slightly smaller Stromgren sphere. This may owe to the gas being slightly cooler in FLEXRT.

Figure 7 shows the spherically averaged temperature profile for $\Delta t = 10 \text{ Myr}$ (left) and 100 Myr (right). At both times, the two modes agree closely with each other behind the I-front. In Generalized Opacity mode, T drops abruptly at the I-front position, since the sharp I-front approximation prevents pre-heating of neutral gas. In Standard mode, there is significant pre-heating ahead of the I-front. By $\Delta t = 100 \text{ Myr}$, the gas is pre-heated to $\sim 10^4 \text{ K}$ to almost the edge of the box. Again, the differences between the modes arise from their different I-front treatments. The temperature profiles behind the I-front in both modes are in broad agreement with the CRTCP codes. Both agree most closely with RSPH and IFT at $\Delta t = 10 \text{ Myr}$, and at $\Delta t = 100 \text{ Myr}$, we find the best agreement with RSPH and CRASH, although the T profile has a slightly different shape than both. The gas in FlexRT is colder close to the source than in C2-Ray, but drops off less quickly approaching the I-front. Ahead of the I-front, Standard mode displays similar levels of pre-heating as RSPH and CRASH. Generalized Opacity mode agrees well with IFT near the I-front.

In Figure 8, we show slices through the temperature around the source using the same format as Figure 5, at $\Delta t = 10$ and 100 Myr . The top two rows compare Standard mode, C2-Ray, and CRASH. The bottom two rows make the same comparison for Generalized Opacity mode, IFT, and FFTE. Standard mode pre-heats the gas ahead of the I-front more than C2-Ray, but less than CRASH, likely because the codes all resolve the high-energy end of the

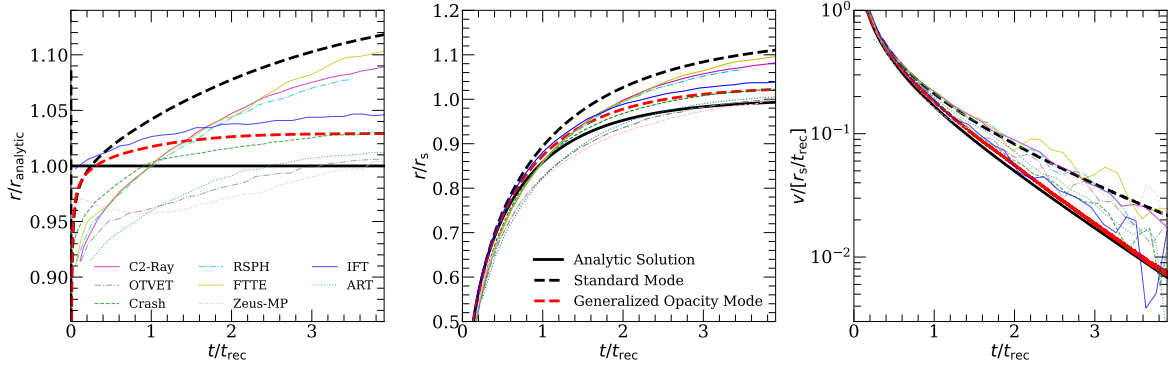


Figure 6. Same as Figure 3, but for Test #2 including temperature evolution. For consistency with I06, we continue to show the constant-temperature ($T = 10^4$ K) analytic solution from Figure 3 as a reference, even though it does not describe the evolving temperature case accurately. The HII region grows larger than the analytic expectation in both modes of FLEXRT, since most of the gas reaches temperatures larger than 10^4 K (and thus has a lower recombination rate). As in Test#1, Generalized Opacity mode produces a smaller HII region. Both modes are in broad agreement with CRTCP results. Standard mode produces a slightly larger Stromgren sphere than the other codes, possibly due to differences in the temperature structure near the I-front and/or differences in how the I-front position is defined (see text). Generalized Opacity mode is close to IFT, but with a slightly smaller HII region.

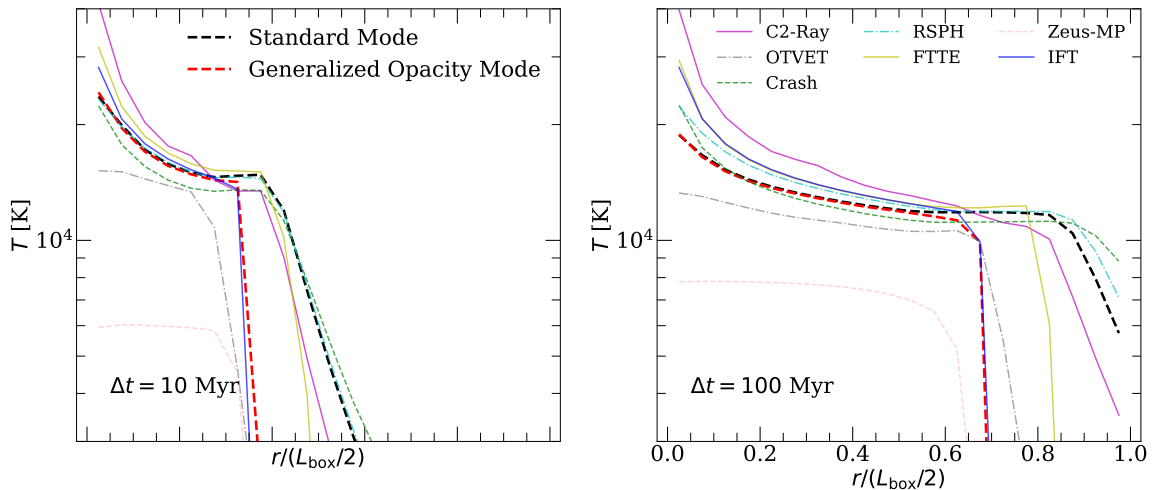


Figure 7. Spherically averaged T profile for Test #2 at $\Delta t = 10$ Myr (left) and 100 Myr (right). Behind the I-front, the FLEXRT modes agree well with each other and the CRTCP results. In Generalized Opacity mode, the temperature drops abruptly ahead of the I-front, since gas there cannot receive any radiation. In standard mode, the hardest ionizing photons pre-heat the neutral gas ahead of the I-front, raising its temperature to $10^3 - 10^4$ K. Behind the I-front, the temperature in FLEXRT is colder than C2-Ray and varies less with distance from the source. Standard mode displays similar levels of pre-heating as RSPH and CRASH. Generalized Opacity mode agrees most well with IFT, as in Figure 4.

spectrum differently. The temperature in C2-Ray is hotter near the source than in FLEXRT and CRASH. This could be due to the lack of collisional ionization cooling in C2-Ray (at the time of writing of I06, see their Table 2, 6th column). The gas near the I-front (edge of

the red/orange region) is hotter in FLEXRT than in CRASH or C2-Ray at $\Delta t = 10$ Myr, suggesting differences in the post-I-front gas temperature. In the bottom two rows, we see that Generalized Opacity mode compares favorably to both IFT and FFTE, since neither of these allow significant pre-heating of the gas ahead of the I-front. The temperature inside the I-front is similar in all three codes at 10 Myr, but is slightly cooler in FLEXRT at 100 Myr than the other codes. This suggests that FLEXRT may have higher equilibrium cooling rates.

Test #2 demonstrates that the two modes of FLEXRT are in good agreement with each other and with the CRTCP codes in terms of thermal physics. As in §5.1, the differences between the two modes of FLEXRT and the CRTCP codes arise mainly from their different I-front treatments, differences in the frequency resolution of the ionizing spectrum, and perhaps differences in the detailed implementation of the heating/cooling physics.

5.3 I-front trapping by a dense clump (Test #3)

Test #3 models the trapping of a cosmological I-front by a dense gas clump embedded in a low-density medium. This test will demonstrate how FLEXRT handles self-shielding and I-front trapping. We use the same setup and test parameters described in §3.4 of I06, which include a 10^5 K blackbody spectrum and a clump that is $200\times$ denser than the gas around it. Figure 9 visualizes the HI fraction at $\Delta t = 1$ Myr and 15 Myr. The layout of the plot is the same as that of Figure 8, with Standard mode compared to C2-Ray and CRASH in the top two rows, and Generalized Opacity mode compared to IFT and FFTE in the bottom two. At $\Delta t = 1$ Myr, the codes in the top row are all similar - there is a thin boundary separating ionized gas on the left edge of the clump from the shadowed interior. At $\Delta t = 15$ Myr, the I-front has penetrated about halfway through the clump and stalled, leaving much of the gas behind the clump still shadowed. The x_{HI} maps are similar in Standard mode and C2-Ray, while in CRASH the I-front doesn't go as far into the clump. I06 attributed this to differences in the spectral energy distribution between CRASH and C2-Ray.

The Generalized Opacity mode compares favorably to the CRTCP codes in the bottom rows. At both $\Delta t = 1$ and 15 Myr, the boundary between ionized and neutral gas is sharper than in the top rows, especially in Generalized Opacity mode. In IFT, the I-front penetrates slightly further into the clump than in Generalized Opacity mode or FFTE, and displays a ring of highly ionized gas round the edge of the clump. Generalized Opacity mode and FFTE are very similar in this comparison. Note that once again, in the ionized part of the clump, Standard and Generalized Opacity modes display similar results.

Figure 10 shows the gas temperature in the same format as Figure 9. At $\Delta t = 1$ Myr, Standard mode and C2-Ray agree well - the gas temperature is $\approx 2 \times 10^4$ K at the left edge of the clump and smoothly decreases to the initial temperature of 40 K near the clump's center. This smooth decline arises due to pre-heating by the hardest ionizing photons. CRASH displays a similar temperature structure, but with the pre-heating penetrating deeper into the clump due to the inclusion of harder ionizing photons in CRASH. At $\Delta t = 15$ Myr, most of the clump has been heated to $T > 10^4$ K, with only a small amount of cold gas remaining at the right edge of the clump. The temperature in the ionized part of the clump is similar in FlexRT and CRASH, while the left edge of the clump is hotter in C2-Ray. This may owe to the lack of collisional ionization cooling in C2-Ray (see §5.2), which is important at these densities and temperatures. The temperature structure behind the clump is similar in all three codes, with $T < 10^4$ K gas behind the shadowed part of the clump and hot gas outside. We see similar results in the bottom rows, with some notable differences. As in Figure 8, Generalized Opacity mode, IFT, and FFTE display very sharp boundaries between hot and

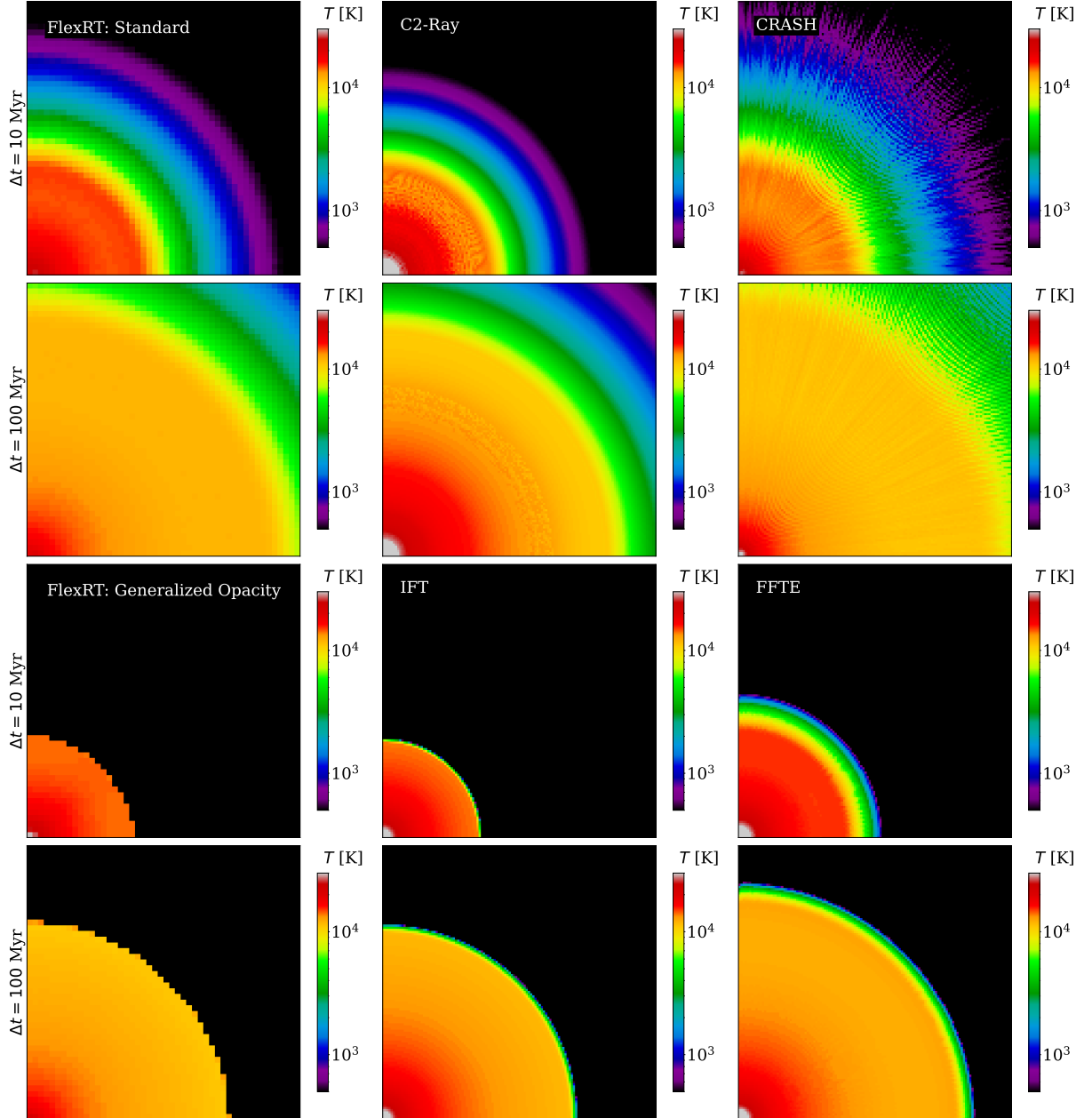


Figure 8. Slices through the gas temperature for Test#2. The 1st and 2nd rows compare Standard mode, C2-Ray, and CRASH (from left to right) at $\Delta t = 10$ and 100 Myr, respectively. The 3rd and 4th rows show the same comparison for Generalized Opacity mode, IFT, and FFTE. The T maps are qualitatively similar in Standard mode, C2-Ray, and CRASH, with FLEXRT displaying more (less) pre-heating ahead of the I-front than C2-Ray (CRASH). This likely owes to differences in the frequency resolution of the ionizing spectrum. Generalized Opacity mode displays no pre-heating due its sharp I-front model, in good agreement with IFT and FFTE. The temperature structure inside the I-front is qualitatively similar in these three codes. The gas is cooler at $\Delta t = 100$ Myr in FLEXRT than the other codes, suggesting it includes more equilibrium cooling.

cold gas, due to their lack of pre-heating. All three codes are very similar at $\Delta t = 1$ Myr. At $\Delta t = 15$ Myr, Generalized Opacity mode and FFTE are also very similar. IFT displays a

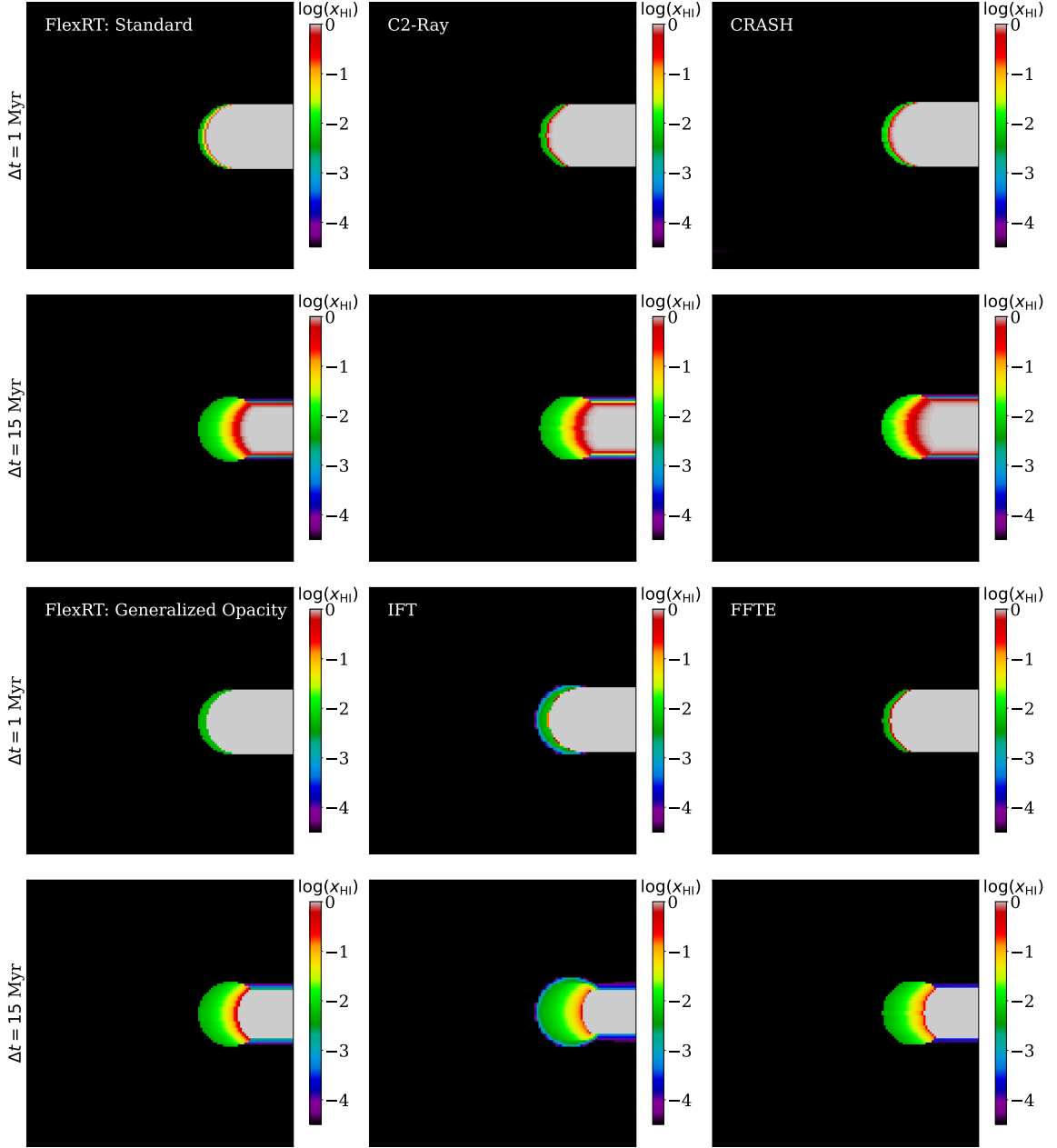


Figure 9. Visualization of x_{HI} for Test #3 - shadowing of a plane-parallel cosmological I-front by a dense clump (see description in text). The layout of the plot is the same as that in Figure 8, with Standard mode compared to C2-Ray and CRASH in the top rows, and Generalized Opacity mode compared to IFT and FFTE in the bottom rows. All codes display fairly similar results at $\Delta t = 1$ Myr - a small amount of gas at the edge of the clump is ionized, with the rest remaining shielded. Again, the boundary between ionized and neutral gas is noticeably sharper in Generalized Opacity mode than in Standard mode, as it is in IFT and FFTE. At $\Delta t = 15$ Myr, the I-front has penetrated about halfway into the clump and stalled. Standard mode and C2-Ray agree well, while in CRASH the I-front doesn't get as far into the clump. Generalized Opacity mode and FFTE are in similarly good agreement, while the front penetrates furthest into the clump in IFT. In these three cases, the boundary between ionized and neutral gas remains sharp throughout.

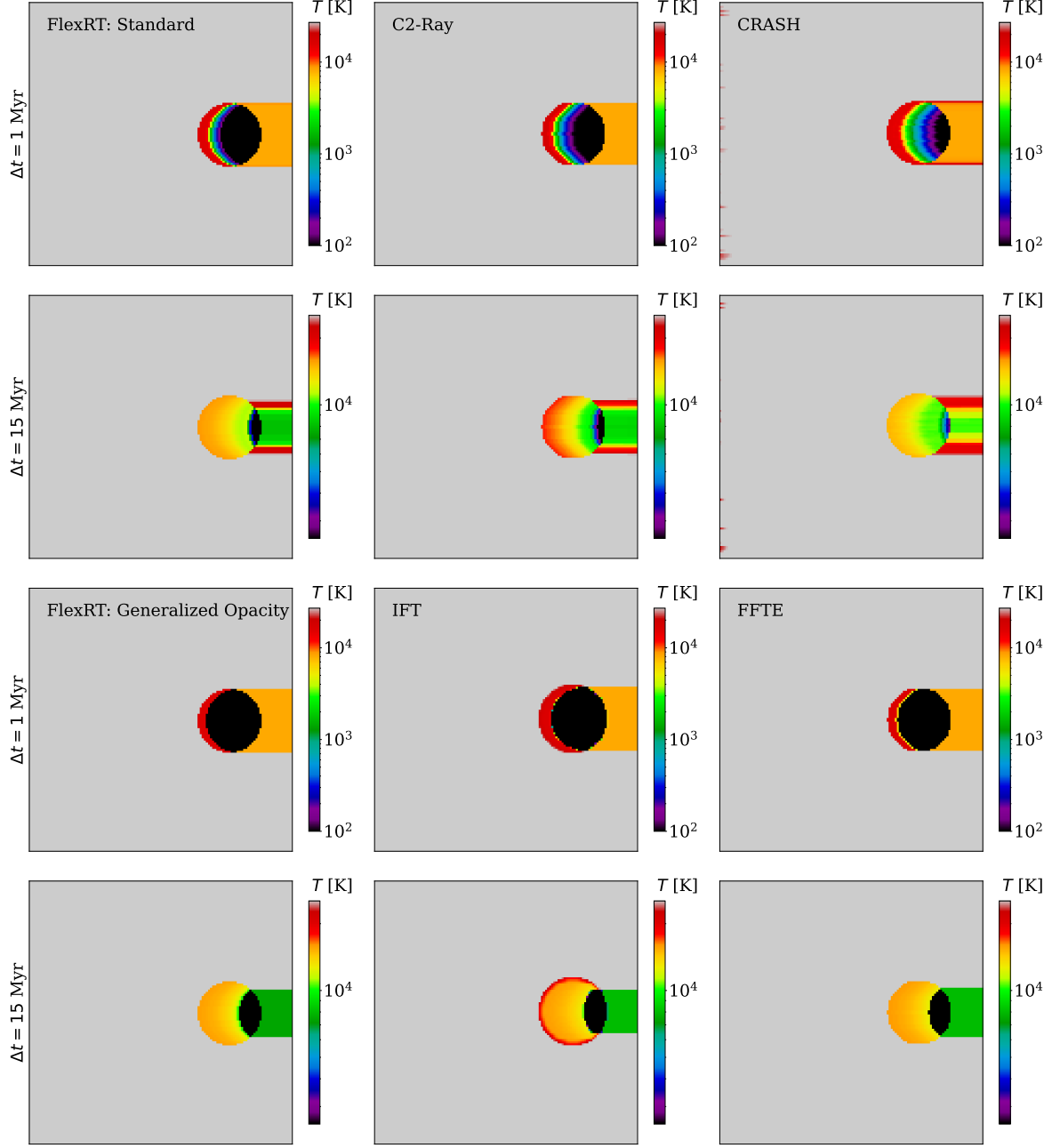


Figure 10. Same as Figure 9, but for gas temperature. The top two rows are qualitatively similar, with Standard mode showing slightly less pre-heating than C2-Ray or CRASH. At $\Delta t = 15$ Myr, the temperature inside the clump is similar in Standard mode and CRASH, but is slightly hotter near the left edge of the clump in C2-Ray. The temperature to the right of the clump is similar in all three codes, with the edges heated by hard photons and the gas in between remaining near its initial temperature. As in Figure 8, we see good agreement in the temperature of Generalized Opacity mode, IFT, and FFTE in the bottom rows. The gas at the left edge of the clump is hot at $\Delta t = 1$ Myr, with no pre-heating behind it. At $\Delta t = 15$ Myr, Generalized Opacity mode and FFT display very similar results, while IFT there is a hot ring around the edge of the clump. The temperature behind the clump is similar in all three codes.

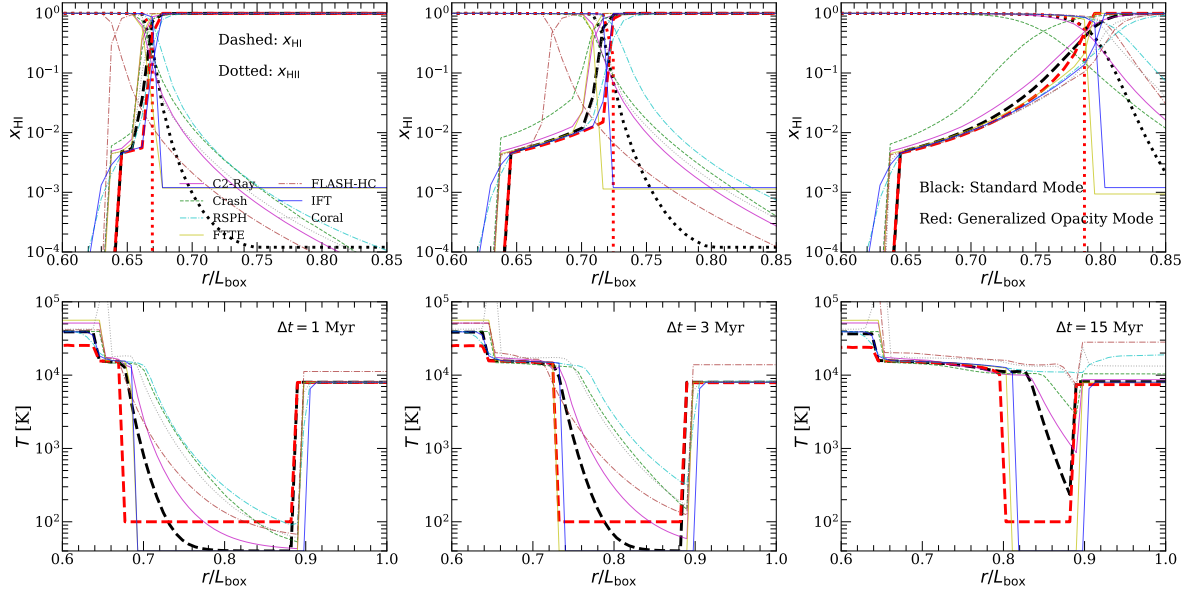


Figure 11. Profiles of x_{HI} (top) and T (bottom) along the symmetry axis of the clump. In the top row, the dashed curves denote x_{HI} and the dotted curves x_{HII} . The x_{HI} profiles behind the I-front inside the clump are in good agreement in Standard and Generalized Opacity mode, as are the I-front positions. In Generalized Opacity mode, there is no ionization behind the front owing to the sharp I-front treatment. The temperature profiles behind the I-front are also similar. In Standard mode, there is significant pre-heating ahead of the I-front, with the whole clump being heated by $\Delta t = 15$ Myr, while Generalized Opacity mode lacks pre-heating entirely. Both codes broadly agree with the CRTCP results. The temperature profiles ahead of the I-front inside the clump differ significantly between the CRTCP codes. The amount of pre-heating in Standard mode is most similar to C2-Ray, while Generalized Opacity mode has no pre-heating and thus best matches FFTE and IFT.

ring of very hot gas around the edge of the clump¹¹, but is otherwise similar to Generalized Opacity mode and FFTE. Again, we note that the temperature of ionized gas is very similar in Standard and Generalized Opacity modes of FLEXRT.

Figure 11 shows the HI (top) and temperature (bottom) profiles cut through the center of the clump along the y direction at $\Delta t = 1, 3,$ and 15 Myr (left to right). We compare against all the codes in I06 (see their Figures 27 and 28). The I-front location and the x_{HI} /temperature profiles behind it in FLEXRT’s two modes agree well with each other. The HI fraction and temperature profiles in FLEXRT broadly agree with the CRTCP results, but there are some notable differences. Behind the I-front, FLEXRT and the CRTCP codes all agree reasonably well. The CRTCP codes differ with each other most in the temperature profile, and associated levels of pre-ionization, ahead of the I-front. Standard mode is most similar to C2-Ray, but differs in that the hardest ionizing photons do not penetrate as far into the clump, which results in less pre-heating of the neutral gas. Generalized Opacity mode is closest to FFTE and IFT, since neither of these codes capture pre-heating. The codes also differ in the temperature of the low-density gas shadowed by the clump. FLEXRT agrees with C2-Ray and IFT, finding that this gas has not yet been heated significantly by $\Delta t = 15$ Myr.

¹¹I06 notes a similar effect for the CORAL code (not displayed here) that arose from inaccuracies in the temperature solver in cells bordering regions with high and low opacity. We speculate that a similar effect may exist in IFT.

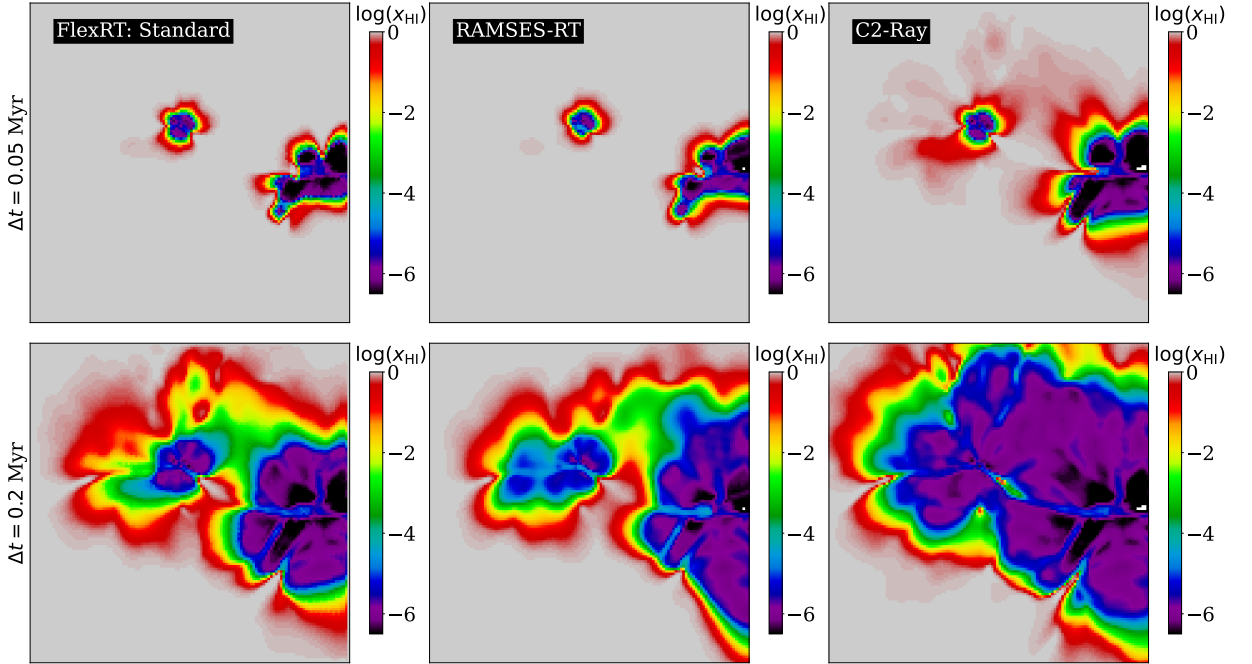


Figure 12. Visualization of x_{HI} for Test #4 - multiple sources in a cosmological density field. We show $\Delta t = 0.05$ Myr and 0.2 Myr in the top and bottom rows (respectively). From left to right, the columns show results for Standard mode, RAMSES-RT, and C2-Ray. The shapes and sizes of the ionized regions in FLEXRT and RAMSES-RT are similar at both times, with some differences in the ionization structure inside them that may arise from differences in the ionization solvers and/or temperature treatments. In C2-Ray, the ionized regions are much larger at both times than in the other two codes, due to its use of the infinite speed of light approximation. However, the ionization state of the gas in the interior of the ionized regions is similar in FLEXRT and C2-Ray, reflecting the similarity of their ionization solvers.

This comparison demonstrates that FLEXRT accurately handles RT and shielding effects in very over-dense regions.

5.4 Test with Cosmological Sources (Test #4)

Our final test in this section is CRTCP Test #4 - a cosmological density field with multiple sources. The setup for this test is described in §3.5 of I06. The box is $0.5 h^{-1}\text{Mpc}$ on a side, and ionizing radiation is emitted from the 16 most massive halos in the box with a constant volume ionizing emissivity of $\dot{N}_\gamma = 8.27 \times 10^{53}$ ph/s/cMpc³. The redshift is fixed to $z = 9$ during the test. In Figure 12, we show slices through the HI fraction at $\Delta t = 0.05$ Myr (top row) and 0.2 Myr (bottom row). From left to right, we show Standard mode, results for the same test using the RAMSES-RT code [48], and C2-Ray. Note that we do not show Generalized Opacity mode here because I06 does not include a realization of Test #4 using IFT, to which Generalized Opacity mode is most directly comparable. We first note that the sizes and shapes of the ionized regions are similar in FLEXRT and RAMSES-RT, while the ionization state of the ionized gas inside differs slightly. This may owe to the different ionization solvers in the two codes. C2-Ray, on the other hand, displays significantly larger ionized regions than the other codes, due to its use of the infinite speed of light approximation (as pointed out by Ref. [48]). The ionization structure deep inside the ionized regions is similar

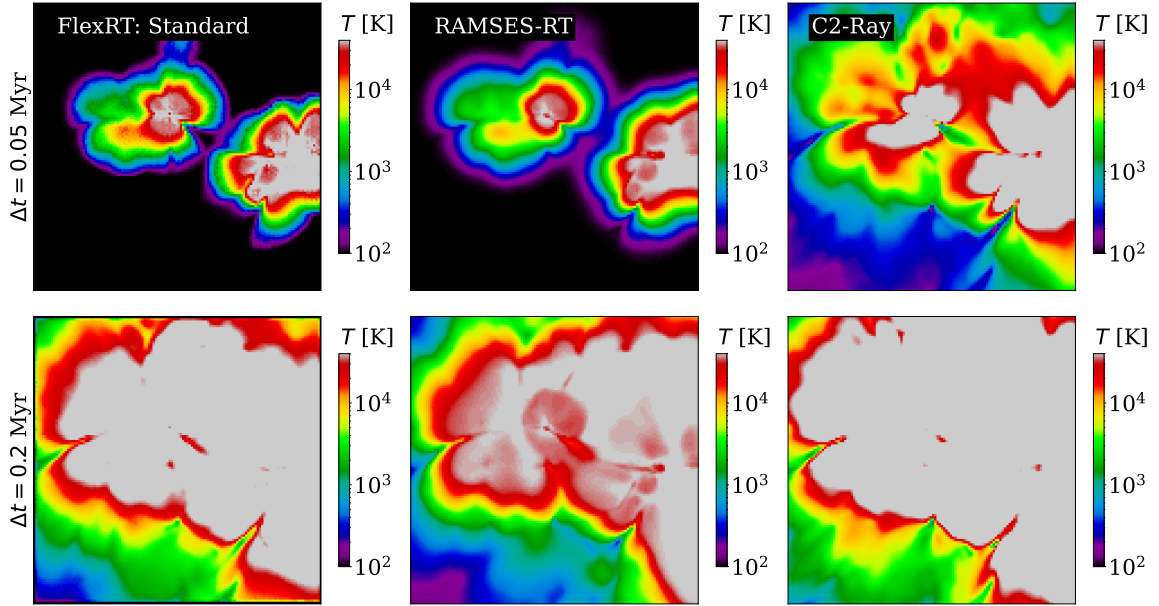


Figure 13. Visualization of temperature for Test #4 with the same layout as Figure 12. The thermal structure in Standard mode is in good qualitative agreement with RAMSES-RT and C2-Ray. The gas inside the highly ionized regions is hot ($T > 3 \times 10^4$ K), and the neutral gas outside is pre-heated by the hardest ionizing photons. The ionized gas in RAMSES-RT is slightly cooler than in FLEXRT and C2-Ray, particularly near the over-dense filaments. The gas near the edges of the box is hotter in C2-Ray since the ionized regions are larger.

in FlexRT and C2-Ray due to the similarity of their ionization solvers.

Figure 13 shows maps of the gas temperature in Test #4 with the same layout as Figure 12. The codes show qualitatively similar results - the gas in ionized regions is very hot ($T > 3 \times 10^4$ K), with layers of progressively colder gas outside the ionized regions. The gradual fall-off in temperature owes, again, to pre-heating by hard photons in the neutral gas. This pre-heating is more significant in C2-Ray than in FLEXRT or RAMSES-RT because of the infinite speed of light. The gas within the ionized regions is slightly cooler in RAMSES-RT than in FLEXRT, possibly due to differences in the binning of ionizing spectrum and/or the implementation of heating and cooling physics.

Figure 14 shows the distributions of x_{HI} (top) and T (bottom) for $\Delta t = 0.05, 0.2,$ and 0.4 Myr (left to right) in Standard mode, RAMSES-RT, and several CRTCP codes. The distribution of x_{HI} in Standard mode agrees well with those of C2-Ray, FFTE, SimpleX, and RAMSES-RT at all times. At $\Delta t = 0.05$ Myr, the normalization is somewhat lower than the CRTCP codes because fewer cells have been ionized in FLEXRT, due to the finite speed of light. The agreement with RAMSES-RT, which also uses the finite speed of light, is much better. At $\Delta t = 0.2$ Myr, the T distribution is similar to that of C2-Ray and RAMSES-RT, reflecting the visual agreement in Figure 13. At $\Delta t = 0.4$ Myr, the location of the high- T peak agrees best with RAMSES-RT, and the shape of the distribution at lower temperatures is intermediate between that of RAMSES-RT and C2-Ray. This suggests that the equilibrium heating/cooling in FLEXRT is closest to RAMSES-RT, and the amount of pre-heating (set by the shape and binning of the ionizing spectrum) agrees well with both codes.

The tests in this section demonstrate that FLEXRT is in broad agreement with previously

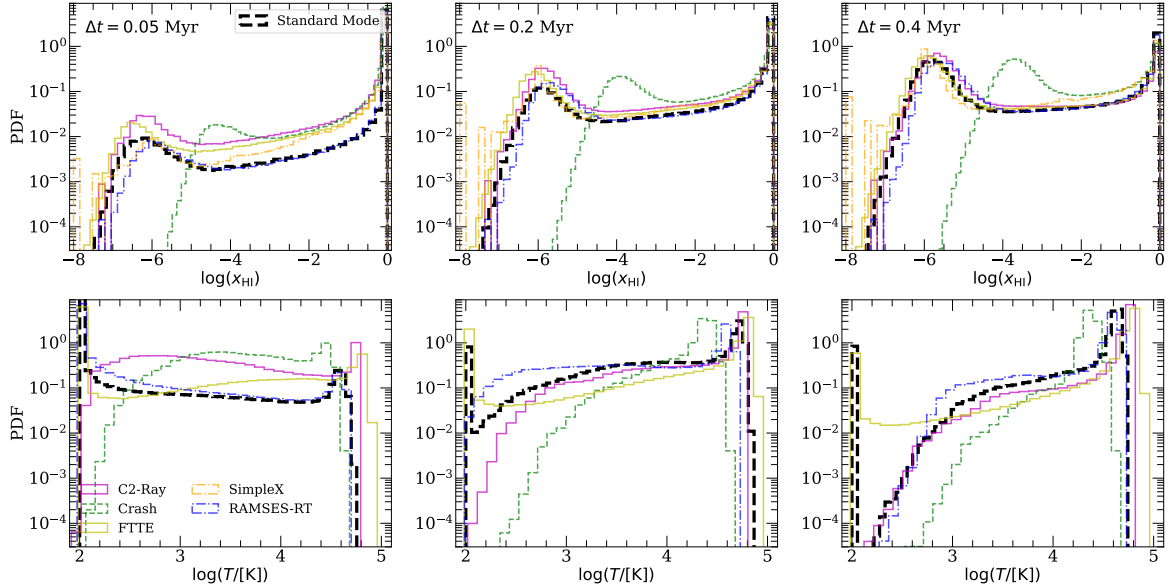


Figure 14. Distribution of x_{HI} (top) and T (bottom) in Test #4 at $\Delta t = 0.05, 0.2,$ and 0.4 Myr (left to right). The shape of the x_{HI} distribution in standard mode agrees well with all the CRTCP codes except CRASH, which has a peak at higher x_{HI} than the other codes. We also find good agreement with RAMSES-RT, especially at $\Delta t = 0.05$ Myr when the finite speed of light is most important. FLEXRT has more cold cells at $\Delta t = 0.05$ and 0.2 Myr than the CRTCP codes due to its finite speed of light (and correspondingly smaller ionized regions), but again we see good agreement with RAMSES-RT. At $\Delta t = 0.4$ Myr, the high- T end of the distribution best matches RAMSES-RT, while the low- T , preheated tail best matches that code and C2-Ray.

tested and validated reionization RT codes in a variety of scenarios. They also highlight some of the important differences between the two modes of FLEXRT. These tests provide key validation for the basic functions of FLEXRT and show that it solves the RT equation accurately in a variety of relevant contexts.

6 Validity of the Moving-Screen I-front method

In the previous section, we noted that the moving-screen I-front approximation employed in Generalized Opacity mode resulted in significant differences with Standard mode in CRTCP tests #1-3. In this section, we address the regime in which this approximation is valid, i.e. the regime in which Standard and Generalized Opacity modes yield very similar results.

The moving-screen I-front approximation assumes that the I-front is entirely unresolved - namely, the typical width of an I-front, Δx_{IF} , is much smaller than Δx_{RT} . To demonstrate this, we have run a cosmological simulation in a $200 h^{-1}\text{Mpc}$ box with a cosmological distribution of halos acting as ionizing sources. The cells in the box have $\Delta x_{\text{RT}} = 1 h^{-1}\text{Mpc}$, considerably larger than the widths of typical cosmological I-fronts ($\Delta x_{\text{IF}} \sim 10-100 h^{-1}\text{kpc}$). The details of this simulation are described in the next section, so we will omit them here - save to emphasize that the moving-screen approximation is expected to be valid in this case because of the large RT cells. The top-left and top-right panels of Figure 15 show maps of x_{HI} (in log scale) for this test in Standard and Generalized Opacity modes, respectively. The inset shows a zoom-in to highlight the structure of the I-fronts. In both cases, the boundary

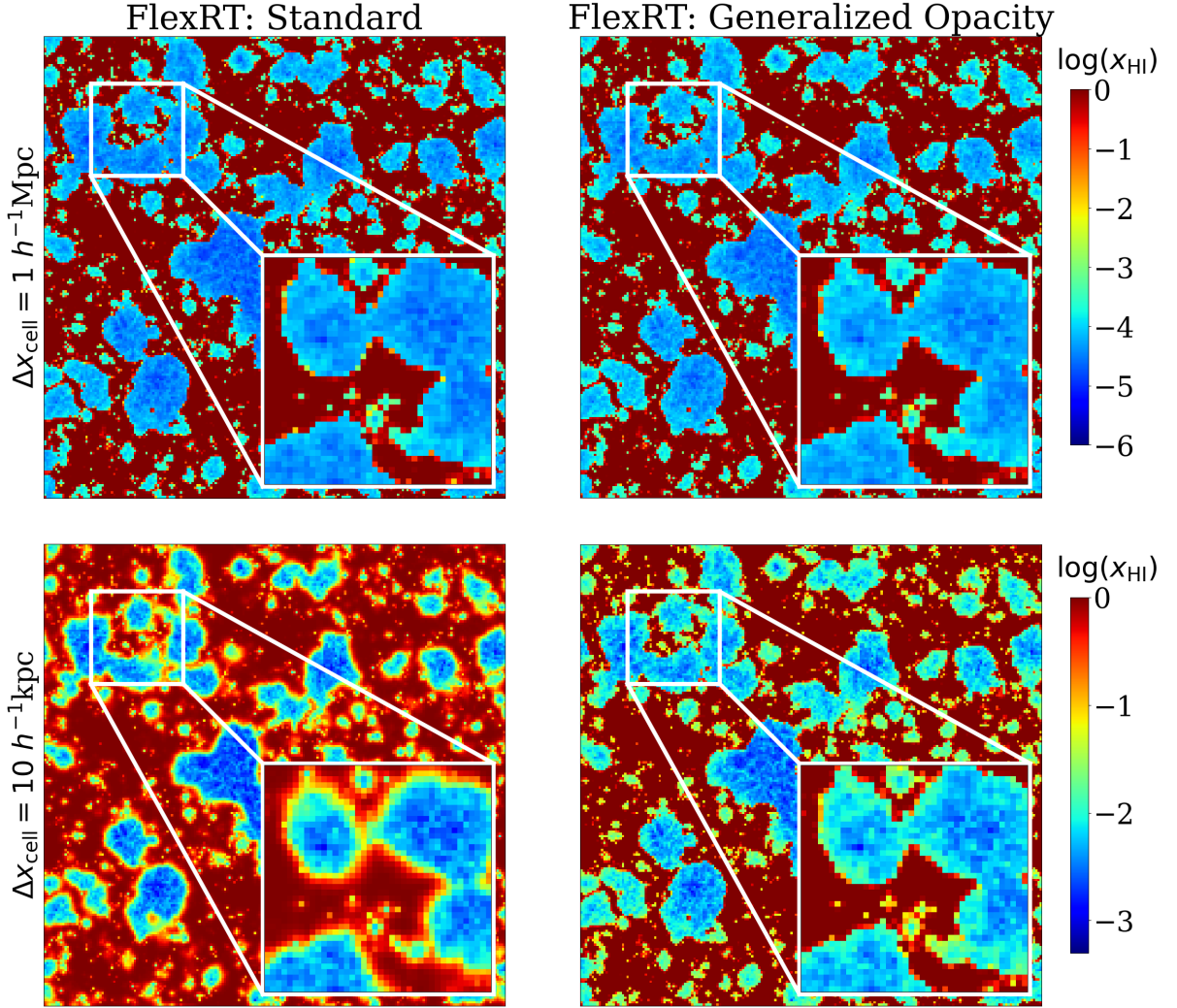


Figure 15. Demonstration of the regime in which the moving-screen I-front approximation used in Generalized Opacity mode is valid. In the top row, we show maps of x_{HI} from a cosmological simulation in a $200 h^{-1}\text{Mpc}$ with $\Delta x_{\text{RT}} = 1 h^{-1}\text{Mpc}$ in both modes. The insets show zoom-ins to highlight the structure of I-fronts. The boundary between neutral (red) and highly ionized (blue/green) cells is one cell thick, indicating that the I-fronts are un-resolved. In this limit, Standard and Generalized Opacity modes produce the same result. In the bottom row, we scale the box volume and ionizing emissivity down by a factor of 100^3 , so that $\Delta x_{\text{RT}} = 10 h^{-1}\text{kpc}$. In this case, the I-fronts are partially resolved in Standard mode (bottom left), differing from the result of the moving-screen approximation seen in the bottom right. This comparison shows that Generalized Opacity mode should be applied in cases where I-fronts are un-resolved. This turns out to be its intended regime of applicability. Conversely, the comparison of the case with large Δx_{cell} shows that the I-front “smearing” effect discussed in §4.1 does not affect the total recombination rate significantly, at least not for this test.

between highly ionized (blue) and neutral (red) cells is only one cell thick, showing that the I-front is un-resolved. The two modes agree very well in this limit.

In the bottom panels, we show a contrasting example in which the moving-screen approximation fails. To do this, we artificially scale the volume of our $200 h^{-1}\text{Mpc}$ box down by a factor of 100^3 so that it becomes a $2 h^{-1}\text{Mpc}$ box. We also scale the ionizing emissivity

of sources down by the same factor so that reionization progresses at the same rate. We then rerun the simulation in the two modes. These runs have $\Delta x_{\text{RT}} = 10 h^{-1}\text{kpc}$, such that I-fronts are partially resolved. We see that in the bottom-left panel, the boundary between highly ionized and fully neutral gas is several cells thick, whereas it remains one cell thick on the bottom-right. This comparison illustrates the regime in which the moving-screen approximation employed in Generalized Opacity mode is valid: $\Delta x_{\text{RT}} \gg \Delta x_{\text{IF}}$. We emphasize that Generalized Opacity mode is designed for large-volume simulations of reionization (see e.g. [21, 35]). Standard mode should be used for problems in which the I-fronts are resolved and their detailed structure is important.

Conversely, our test shows that in the case with $\Delta x_{\text{RT}} = 1 h^{-1}\text{Mpc}$, the growth of ionized regions is largely unaffected by the error in the recombination rate inside I-fronts incurred in Standard Mode (see discussion in S4.1). This suggests that, at least in this test, the recombinations taking place in partially ionized cells do not contribute significantly to the total ionizing budget in the simulation. However, we caution that this result may not hold in the case where the recombination rate is being boosted at the sub-grid level to account for missing small-scale structure. In general, a test like the one shown in this section - comparing the moving-screen method to the Standard Mode procedure - can be used to assess the importance of such recombinations and determine if the treatment in Standard Mode is sufficiently accurate for a given situation.

7 Testing the Merging Scheme

In §5, we demonstrated good qualitative and quantitative agreement between FLEXRT and the CRTCP codes. Those tests validate the basic functionality of FLEXRT, including ray transport and splitting, absorption, gas chemistry, and thermal evolution. However, none of them employ one of the key speed-up mechanisms in FLEXRT: ray merging. Indeed, we turned off merging in all of those tests to enable a maximally clean comparison to the CRTCP results. In this section, we describe two more tests designed to validate the merging scheme in FlexRT. In §7.1, we will re-visit the CRTCP cosmological test, this time with merging included. In §7.2, we run a cosmological test on a much larger scale and directly compare to results from the RADHYDRO code of Ref. [47], which uses a similar ray merging approach.

7.1 CRTCP Test #4 (again)

We return here to CRTCP Test #4, but this time vary the parameters that control merging, which are described in §3.3. We consider a case where rays adaptively split but do not merge (“No Merging”), and two scenarios with merging, both of which track 12 unique directions for merged rays (that is, $l_{\text{merge}} = 0$). We set the number of rays per cell exempt from merging, N_{ex} , to 16 for one run and 4 for the other. Both runs have $N_{\text{ray}}^{\text{min}} = 2$ (Eq. 3.2). In the case with $N_{\text{ex}} = 16$, the box can reach \approx half ionized before rays begin merging. Since rays are rank-ordered for by their photon counts to determine if they will be exempt from merging, only rays near the edges of ionized regions will be merged in this case. For $N_{\text{ex}} = 4$, rays begin merging when the box is only 1/8th ionized, and by the end of the simulation most rays are eligible for merging. Importantly, the $N_{\text{ex}} = 4$ ran ≈ 7 times faster and requires a factor of ≈ 2 less memory than the No Merging case, reflecting the significant computational savings afforded by merging.

Figure 16 shows the global ionized fraction vs. time (top left) and mean photo-ionization rate Γ_{HI} (top right) for these three runs. The solid and dashed curves denote volume and

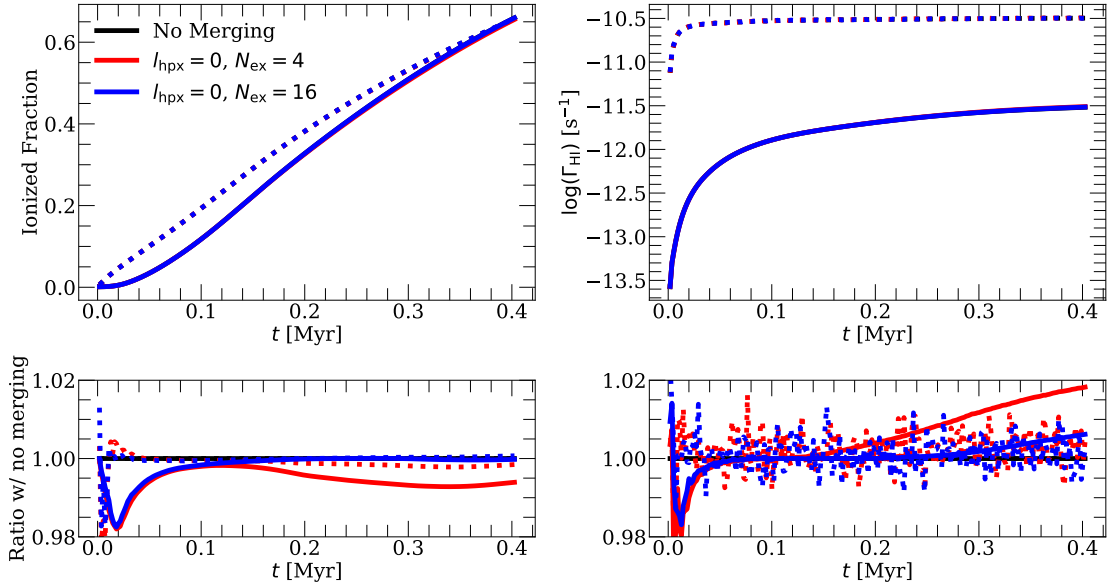


Figure 16. Mean ionized fraction and Γ_{HI} in versions of Test #4 with different merging parameters. Solid (dotted) curves denote volume (mass)-weighted averages. The black curve has no merging, while for the red curve we allow for aggressive ray merging that speeds up the calculation by a factor of ≈ 7 . The blue curve is an intermediate case. The bottom panels show the ratios of each quantity with the no-merging run. We find 1 – 2% level agreement at all times in these quantities for very different merging scenarios.

mass-weighted averages. The bottom panels show the ratio of the $N_{\text{ex}} = 4$ and 16 cases with the No Merging case. We see that the curves mostly overlap in the top panels. The bottom panels show that the differences between the averaged quantities are at most 1 – 2% in all cases, demonstrating that merging has a small effect on globally averaged quantities¹².

We show slices through the x_{HI} (top) and Γ_{HI} (bottom) fields in Figure 17, with the No Merging, $N_{\text{ex}} = 4$, and $N_{\text{ex}} = 16$ models shown from left to right. The No Merging and $N_{\text{ex}} = 16$ cases have similar x_{HI} fields. A modest amount of noise is seen in the Γ_{HI} field for the latter, particularly near the edges of ionized regions. In the $N_{\text{ex}} = 4$ case, however, the Γ_{HI} field is quite noisy, and some of the noise is visible in the x_{HI} field. This is primarily shot noise caused by the relatively small number of rays (and independent directions) being tracked. Importantly, the structure of the ionized bubble, and the large-scale fluctuations in x_{HI} and Γ_{HI} , are mostly unaffected by the shot noise even for $N_{\text{ex}} = 4$. This demonstrates that over many time steps, the effects of this noise average out and have little effect on the growth of ionized regions or the large-scale features of the radiation field. The insensitivity of large-scale gas properties to this noise is encouraging, since in many cosmological contexts only the large-scale features of the radiation field are important for modeling observables (e.g. the 21 cm signal [42] and large-scale fluctuations in the Ly α forest [17]).

7.2 Test against RADHYDRO

In this section, we test FLEXRT against the RADHYDRO code of Ref. [47], which has a ray tracing algorithm similar to FlexRT (including merging). We use a box with length

¹²The $\sim 2\%$ differences at the beginning of the sims may arise from different choices for random rotations of the rays in the ray casting scheme - see §3.1.

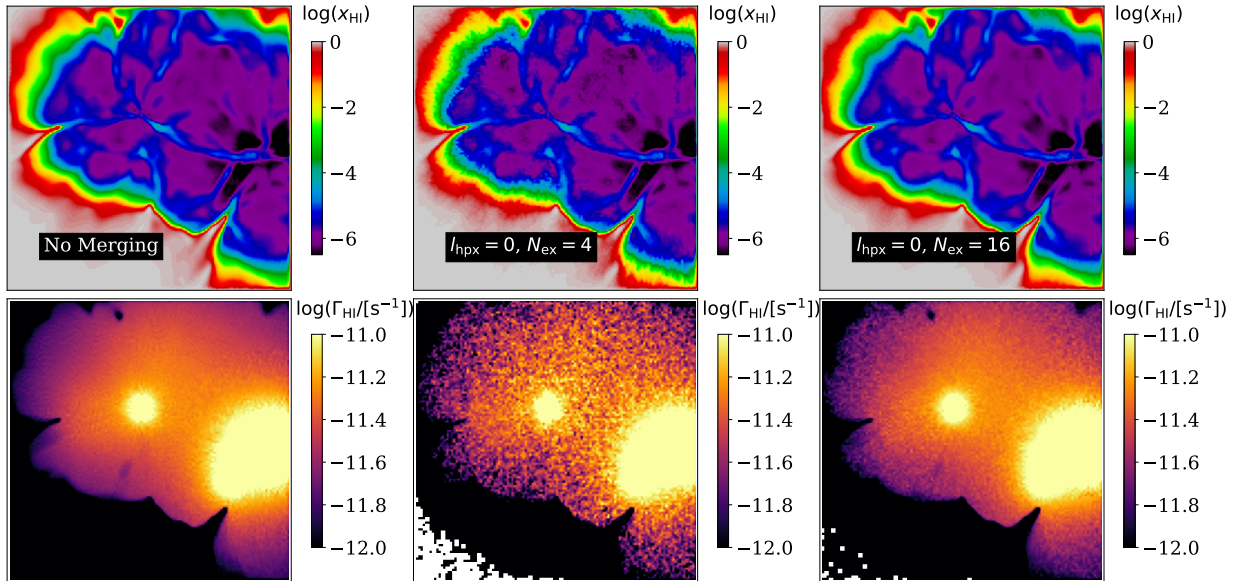


Figure 17. Visualization of the HI fraction (top) and Γ_{HI} (bottom) for the merging scenarios shown in Figure 16. In the “no merging” case, both fields are smooth. The second case displays significant shot noise in the Γ_{HI} field due to the sparsity of rays, which is also visible (to a lesser degree) in the x_{HI} field. The third case shows intermediate results, with a small amount of noise visible in the Γ_{HI} near the edges of ionized regions. Crucially, the large-scale fluctuations in Γ_{HI} and x_{HI} and the structure of the ionized bubble remain similar to the no merging case even with aggressive merging, suggesting that these large-scale features are mostly insensitive to small-scale noise caused by merging.

$L = 200 h^{-1}\text{Mpc}$, large-enough to capture realistically the clustering of dark matter halos. We first run an N-body simulation with $N = 3600^3$ particles to get dark matter halos with masses $\geq 3 \times 10^9 h^{-1}M_{\odot}$, which become the sources for our RT simulation. Next, we run a hydrodynamics simulation using the same initial density fluctuations and $N = 1024^3$ gas cells, and smoothed the gas density field to $N = 200^3$ for the RT calculation. We use a single snapshot of the halo field at $z = 7$ for the simulation, and post-process the density field at that redshift with an ionizing emissivity per unit volume¹³ of $\dot{N}_{\gamma} = 7.96 \times 10^{50}$ ph/s/cMpc³. For simplicity, we set the gas temperature to a constant $T = 10^4$ K. Our splitting parameters for our fiducial FLEXRT run are $l_{\text{source}} = 1$ and $N_{\text{ray}}^{\text{min}} = 2$, and our merging parameters are $l_{\text{merge}} = 1$ and $N_{\text{ex}} = 16$. These choices give a reasonably close match to the default splitting/merging scheme parameters used in RADHYDRO (see Ref. [47] for details). We have also run a “High-res” simulation with FLEXRT that has $N_{\text{ex}} = 128$.

We show the ionized fraction as a function of time in the top panel of Figure 18 for RADHYDRO (black) and FLEXRT (blue), and their ratio in the bottom panel. The solid (dashed) lines denote volume (mass)-weighted averages. The differences between FLEXRT and RADHYDRO are a few percent or less. The slight disagreement may arise from the codes’ different ionization solvers. Specifically, RADHYDRO assumes the optically thin limit of Eq. 4.1 and does not account for evolution of the neutral fraction during a time step (Eq. 4.2-4.6) when calculating the opacities of cells. This is an important difference for our test setup because the large RT cells ($1 h^{-1}\text{Mpc}$) result in large opacities in partially neutral

¹³Halos are assigned UV luminosities by abundance-matching to the UV luminosity function of Ref. [92], and emissivities of individual halos are proportional to their luminosities.

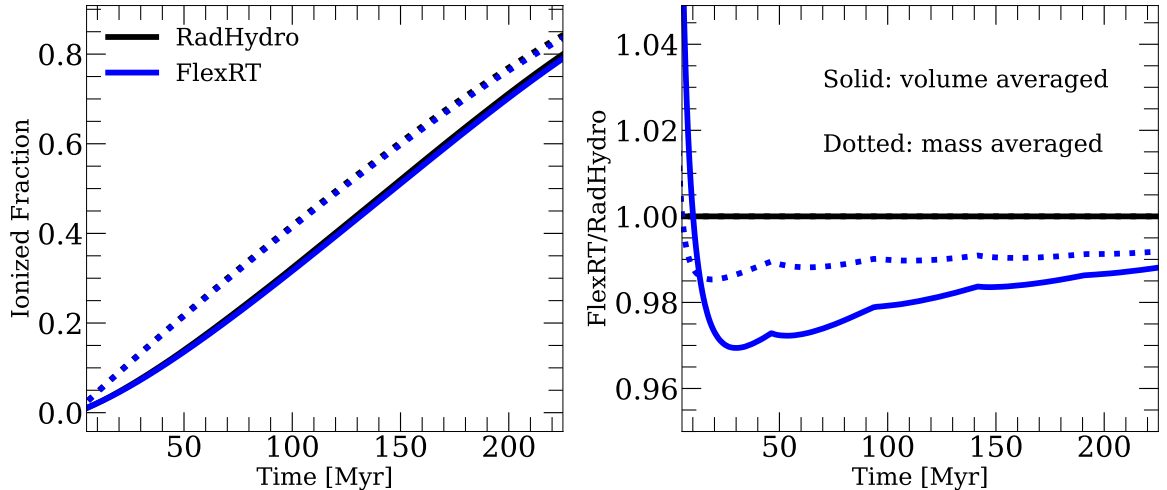


Figure 18. Evolution of the ionized fraction with time in our comparison test of FLEXRT (black) and RADHYDRO (blue). Solid (dashed) curves denote volume (mass)-weighted averages. The bottom panel shows the ratio of the FLEXRT and RADHYDRO results. The ionization history in FLEXRT lags 2 – 3% percent behind that of RADHYDRO, possibly due to differences in the codes’ ionization solvers.

cells ($\tau \gg 1$) and large time steps ($\Delta t = 0.6$ Myr). Another, related effect could be that of HealPix structural artifacts, discussed in §3.1. RADHYDRO does not randomly rotate the HealPix spheres used to cast rays on every time step¹⁴. This could lead to differences in the recombination rate around isolated sources early in the simulation before ionized regions overlap.

Figure 19 visualizes the ionization field for RADHYDRO (top) and FLEXRT (middle) at volume-averaged ionized fractions of 20%, 50%, and 80% (left to right). White (black) regions denote ionized (neutral) gas. The bottom panels show the linear differences between the codes, with blue (red) regions being more neutral in RADHYDRO (FLEXRT). We find excellent agreement in the morphology of ionized regions at all three ionized fractions. Indeed, the maps are so similar that we must refer to the difference maps to easily detect differences. At 20% ionized, the largest ionized bubbles are slightly smaller (more neutral) in FLEXRT, as indicated by their mostly red boundaries. Smaller ionized bubbles, on the other hand are more neutral in RADHYDRO (that is, they have blue boundaries). The opposite is true in the other two maps. The prominent blue boundaries of neutral islands at 80% ionized reflect that the two maps are not at exactly the same ionized fraction (80% vs. 82% for RADHYDRO and FlexRT, respectively). These slight, small-scale morphological differences may arise from differences in the codes’ ionization solvers, and/or differences in ray splitting/merging.

Figure 20 quantifies the agreement in the ionization field. The top row shows the dimensionless power spectrum of the ionization field fluctuations vs. k for the same ionized fractions in Figure 19. The black solid, red dotted, and blue dashed curves show the auto power for FLEXRT and RADHYDRO, and their cross-power, respectively. In the bottom panels, we

¹⁴Instead, it assigns each source a single set of random rotation angles, which are used throughout the simulation.

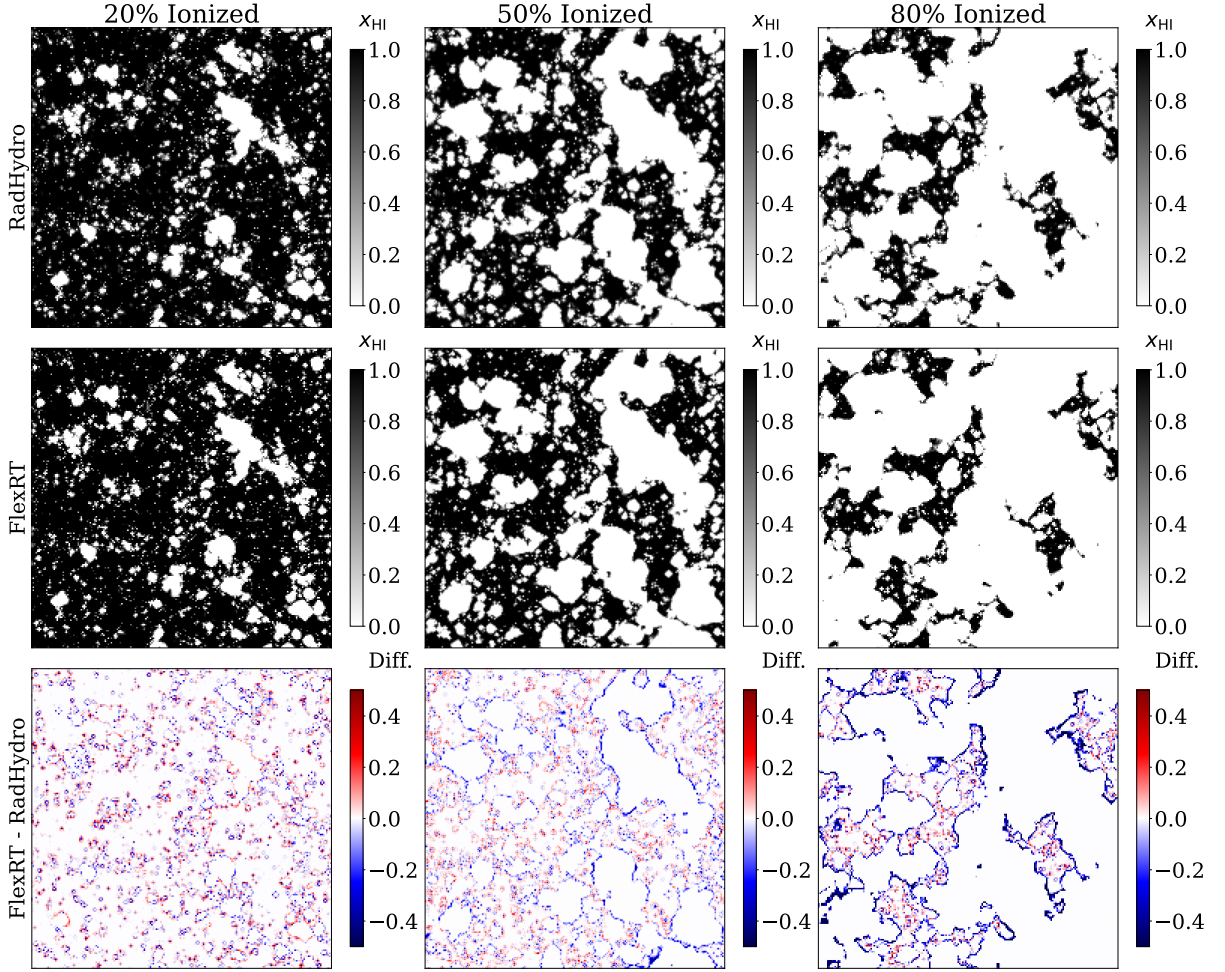


Figure 19. Slices through the neutral fraction field from RADHYDRO (top) and FLEXRT (middle) at 20%, 50% and 80% volume ionized fractions (left to right). Black (white) regions are neutral (ionized). The bottom row shows the difference between the two. Blue (red) cells have higher neutral fractions in RADHYDRO (FLEXRT). At fixed ionized fraction, the large-scale features of the ionization field are in very good agreement. Inspection of the difference maps reveals slight morphological differences between the codes, especially at 80% ionized - see text for details.

show the correlation coefficient, defined as

$$r(k) = \frac{P_{\text{FLEXRT,RADHYDRO}}(k)}{\sqrt{P_{\text{FLEXRT}}(k)P_{\text{RADHYDRO}}(k)}} \quad (7.1)$$

where the numerator is the cross-power and the denominator contains the auto terms. For perfectly correlated (un-correlated, anti-correlated) fields, $r(k) = 1$ (0 , -1). The shaded region in the bottom panel denotes a 10% deviation from unity. At 20% and 50% ionized, the FLEXRT and RADHYDRO ionized fields are almost perfectly correlated at all scales, with a 5 – 10% deviation emerging only near the Nyquist wavenumber ($\approx 3 \text{ hMpc}^{-1}$). At 80% ionized, 5 – 10% deviations from $r = 1$ are evident at $k > 0.3 \text{ hMpc}^{-1}$. RADHYDRO also has slightly more power on nearly all scales. These differences are likely due to differences in how rays are merged (see subsequent discussion) and the slight mis-match in the ionized fractions of the 80% ionized outputs.

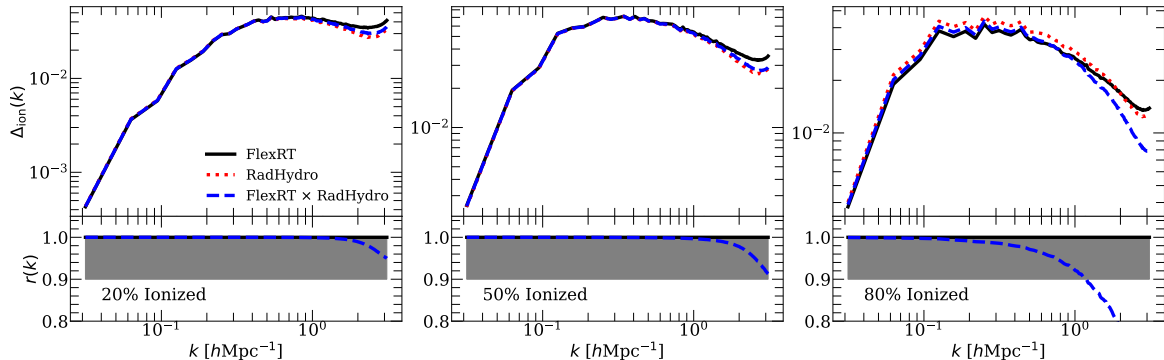


Figure 20. Top: auto power spectrum of the ionization field $\Delta_{\text{ion}}(k)$ for FLEXRT and RADHYDRO (solid black and dotted red), and their cross-correlation (dashed blue). Bottom: their cross-correlation coefficient, $r(k)$ (Eq. 7.1). From left to right, the columns show results at 20%, 50%, and 80% ionized. At 20% and 50% ionized, the power spectra are almost indistinguishable, with $r(k)$ differing from unity only close to the Nyquist wavenumber ($k_{\text{nyq}} = \pi/\Delta x_{\text{RT}} \approx 3 \text{ hMpc}^{-1}$). At 80%, the codes are still in good agreement, but RADHYDRO has slightly more ionization power at intermediate scales. This is probably due to differences in how the codes handle ray merging as the ionized fraction nears unity.

We next consider the large-scale fluctuations in the Γ_{HI} field, which are important to capture correctly for a number of reionization applications (e.g. the Ly α forest, [17, 93]). Figure 21 visualizes the fluctuations in Γ_{HI} in the same format as the ionization fluctuations in Figure 19. In this case, the bottom row shows the ratio (logarithmic difference) of the fields. The locations of the ionizing sources, near the centers of ionized bubbles, can be identified by the bright spots in the Γ_{HI} maps. At 20% ionized, the Γ_{HI} fluctuations closely trace the ionization fluctuations. At 50% ionized, some additional structure is visible within ionized regions, which traces the spatial distribution of the ionizing sources. In both cases, the codes are in good agreement. At 80% ionized, some differences are evident. First, both codes begin to display noise in the Γ_{HI} field, which arises from merging (see Figure 1 and discussion). The noise is slightly more noticeable in FLEXRT than RADHYDRO, suggesting that FLEXRT is tracking fewer rays¹⁵. However, we also see differences on larger scales in this comparison. The ratio map shows that ionized regions generally have higher Γ_{HI} in FlexRT, especially at the edges of ionized bubbles. This could be partially due to the slight mismatch in neutral fractions mentioned earlier. It also may be that the merging of rays is beginning to affect large-scale Γ_{HI} fluctuations. Recently, Ref. [65] argued that Γ_{HI} fluctuations on scales smaller than the ionizing photon mean free path could be affected by differences in the angular resolution of the radiation field (see their Fig. 3 and related discussion). Since FlexRT and RADHYDRO do not parameterize or treat merging in exactly the same way, large-scale fluctuations in the codes might be affected differently.

Figure 22 compares the power spectrum of Γ_{HI} , $\Delta_{\Gamma}(k)$, in the same format as Figure 20. At 20% ionized, $\Delta_{\Gamma}(k)$ has almost the same shape as $\Delta_{\text{ion}}(k)$, since the early fluctuations in Γ_{HI} are dominated by fluctuations in the ionization field. Unsurprisingly, FLEXRT and RADHYDRO agree very well, as they do in Figure 20. At 50% ionized, the shape of $\Delta_{\Gamma}(k)$ begins to differ from that of $\Delta_{\text{ion}}(k)$, peaking at slightly smaller k . This is because the largest

¹⁵Recall from Figure 2 that the number of rays in FlexRT does not saturate quite to $N_{\text{ray}}^{\text{max}}$, whereas in RADHYDRO it does. This may account for the slightly higher noise in FlexRT

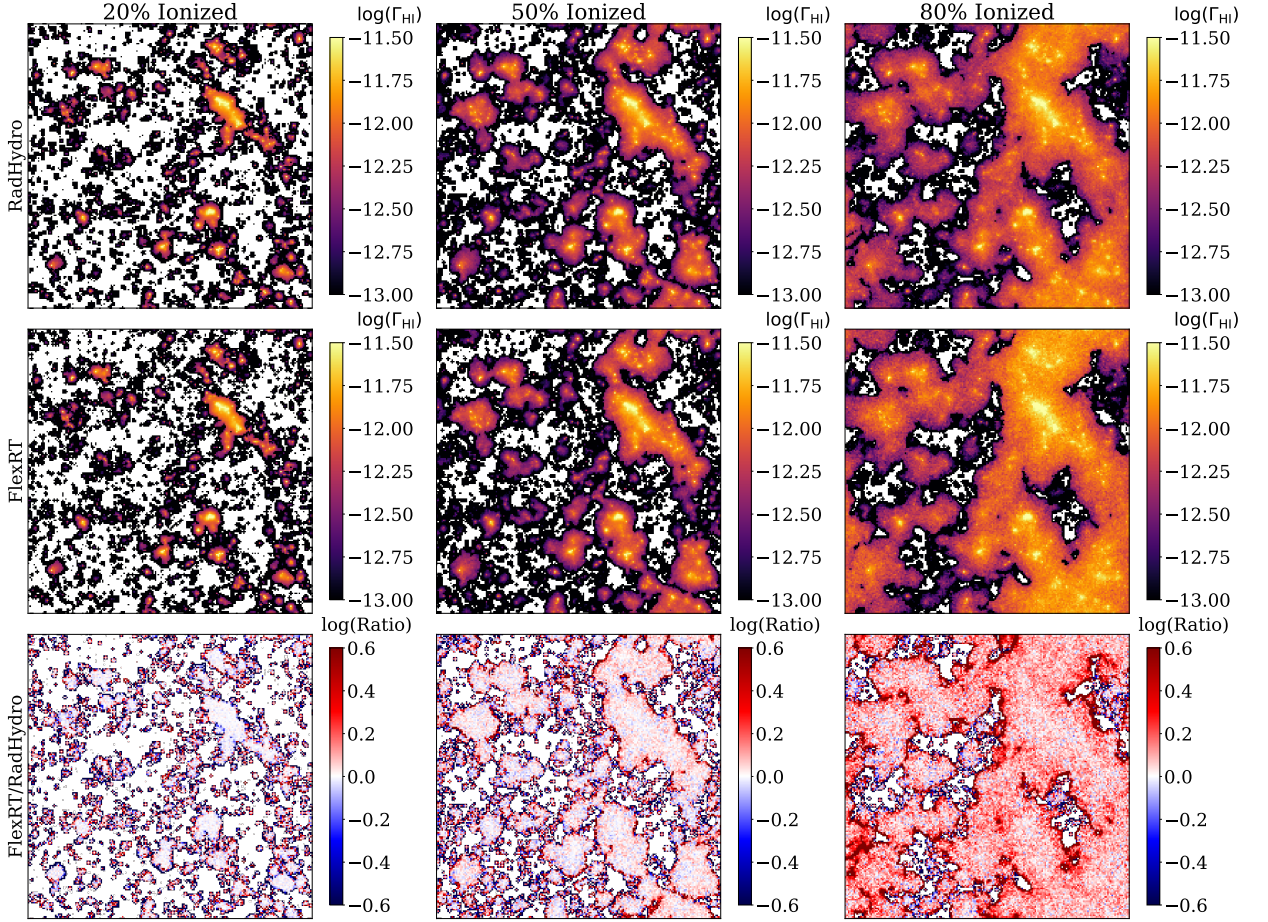


Figure 21. Visualization of the Γ_{HI} fields in RADHYDRO and FLEXRT, in the same format as Figure 19. The bottom panel shows the ratio (logarithmic difference) in Γ_{HI} . Note that blue (red) regions have higher Γ_{HI} in RADHYDRO (FLEXRT). At 20% ionized, the Γ_{HI} fluctuations almost completely trace the ionization fluctuations. At 50% ionized, some additional structure within ionized regions becomes evident, tracing the clustering of the sources. RADHYDRO and FLEXRT are indistinguishable in these cases. At 80% ionized both Γ_{HI} fields start to show small-scale noise, arising from merging (see Figure 1 and discussion). In the difference map, we also see some differences on larger scales, with FLEXRT having higher Γ_{HI} , especially near the edges of ionized regions.

ionized bubbles also have the brightest sources, and hence the largest Γ_{HI} . This enhances large-scale power in the Γ_{HI} field relative to the ionization field. Again, the level of agreement between FLEXRT and RADHYDRO is similar to that in Figure 20, showing that FLEXRT is capturing the large-scale Γ_{HI} fluctuations correctly.

At 80% ionized, the peak in $\Delta_{\Gamma}(k)$ has moved to yet smaller k , approaching the box scale. The power also drops off more rapidly at small scales, since ionized bubbles have begun overlapping and the UVB has started to homogenize. The up-turn at $k > 1 \text{ hMpc}^{-1}$ is due to shot noise in the radiation field due to ray merging. This noise is visible in the Γ_{HI} maps for both codes, but is slightly more prominent in FLEXRT. From the bottom panel, we see that the correlation between the codes is slightly worse than it was for the ionization maps. The drop-off in $r(k)$ at large k coincides with the up-turn in power at large k , reflecting the “ray noise” discussed previously. FLEXRT also has slightly less power at $0.3 < k < 1 \text{ hMpc}^{-1}$,

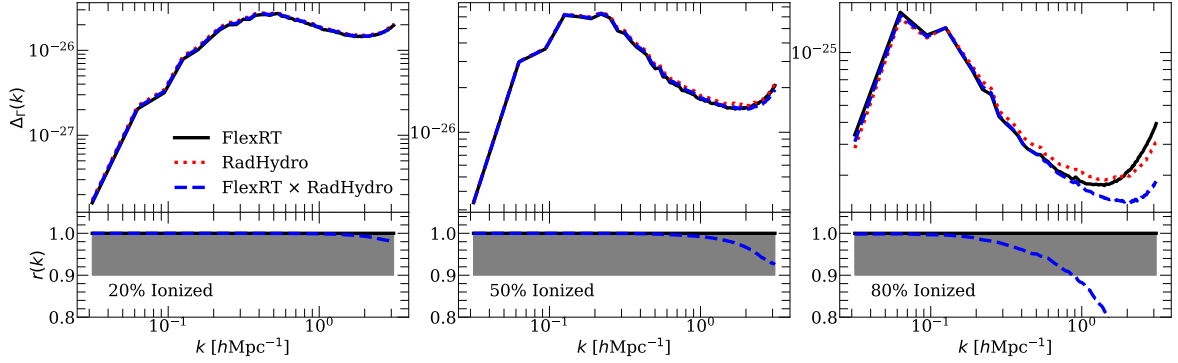


Figure 22. Power spectra of Γ_{HI} , Δ_{Γ} , in the same format as Figure 20. At 20% ionized, Δ_{Γ} has nearly the same shape as Δ_{ion} , and the codes match just as well. At 50% ionized, Δ_{Γ} peaks at a smaller k than Δ_{ion} due to fluctuations within large ionized bubbles, and the codes remain in tight agreement. At 80% ionized, we see a significant up-turn at large k in both codes due to shot noise from merging, which is slightly more significant in FLEXRT. FLEXRT also has slightly less power at $0.3 < k/[h\text{Mpc}^{-1}] < 1$. The $r(k)$ is slightly worse than for the ionization field (Figure 20).

reflecting the differences at large-scales discussed above.

Figure 23 shows the residual HI fraction (left), Γ_{HI} (middle), and the reionization redshift (z_{reion}) field (right) just after reionization has finished (100% ionized). The third row shows a higher-resolution version of the FlexRT test, with $N_{\text{ex}} = 128$. The bottom row shows ratio maps for x_{HI} and Γ_{HI} , and a difference map for z_{reion} , for the fiducial resolution FLEXRT run and RADHYDRO. We show Γ_{HI} normalized by its mean value to more easily compare spatial fluctuations. Fluctuations in the HI fraction on intermediate scales are mainly set by the density field ($x_{\text{HI}} \propto \Delta$), which is the same in both codes, so we see good agreement in the left panels. However, the large-scale features in Γ_{HI} differ noticeably between FlexRT and RADHYDRO, as highlighted by the large-scale features visible in the ratio maps. We have checked, by running tests in boxes with fewer RT cells and much higher ray tracing resolution, that these large scale differences arise from merging - that is, the codes converge to the same answer in the no-merging limit.

Figure 24 shows the power spectrum of the residual HI fraction $\Delta_{\text{HI}}(k)$ (left) and $\Delta_{\Gamma}(k)$ (left) at 100% ionized. The dot-dashed lines show results for the high-resolution FlexRT simulation. The bottom row shows $r(k)$. At intermediate scales ($0.1 < k/[h\text{Mpc}^{-1}] < 1$), where density fluctuations dominate the fluctuations in x_{HI} , we find good agreement in $\Delta_{\text{HI}}(k)$. However, $\Delta_{\Gamma}(k)$ is appreciably different on all scales, with $r(k) \lesssim 0.8$. RADHYDRO has more power than both of the FlexRT runs at $k < 0.5 h\text{Mpc}^{-1}$. The up-turn at small k in both codes is due to shot noise, which is more (less) prominent in the fiducial (high-resolution) FLEXRT run than in RADHYDRO. Although the precise reason for the differences at larger scales is unclear, we are sure that they arise in some way due to merging. We have confirmed that in tests without any merging, FlexRT and RADHYDRO give nearly identical Δ_{Γ} .

The fact that different ray merging schemes can result in differing large-scale Γ_{HI} fluctuations after reionization ends is of potential concern for applications that are sensitive to these fluctuations. These include the Ly α forest of high-redshift quasars [16, 93]. As we showed in Figure 1, this noise can be mitigated by increasing the number of directions tracked (parameterized by l_{pix}) and exempting more rays from merging (controlled by N_{ex}). Adjusting these parameters will help to mitigate the ray noise, at the cost of computational efficiency.

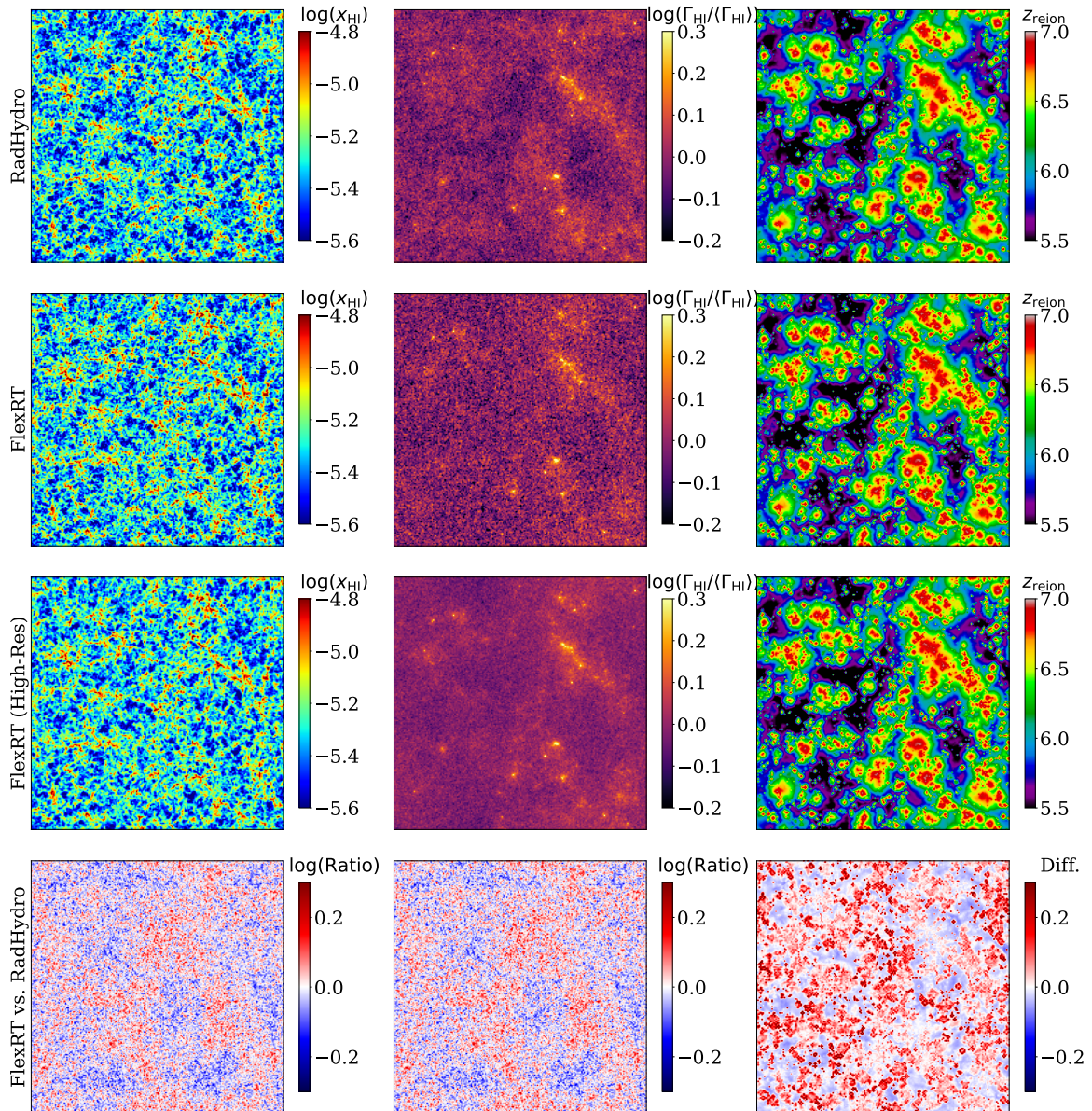


Figure 23. Visualization of gas properties after the completion of reionization (100% ionized). From left to right, we show the residual x_{HI} , Γ_{HI} , and the reionization redshift (z_{reion}) field. The third row shows a high-resolution version of the FlexRT run, with $N_{\text{ex}} = 128$. The bottom row shows ratio maps for the x_{HI} and Γ_{HI} fields and a difference map for the z_{reion} fields (using the high-resolution FlexRT run). Fluctuations in x_{HI} are dominated by density, so they agree well between the codes. The Γ_{HI} fields are similar, but with shot noise now conspicuous. There is more (less) noise in the fiducial (high-res) FlexRT run than in RADHYDRO. We also see that FlexRT shows less significant large-scale fluctuations in its Γ_{HI} field (for both resolutions). The z_{reion} fields are in excellent agreement, showing their relative insensitivity to the effects of merging. In addition to small-scale noise, some large-scale features are notable in the ratio maps of Γ_{HI} . The z_{reion} difference map betrays minor differences in ionized morphology and reionization history. Small bubbles embedded in late-ionizing regions tend to ionize earlier in FLEXRT, and the surrounding voids ionize earlier in RADHYDRO.

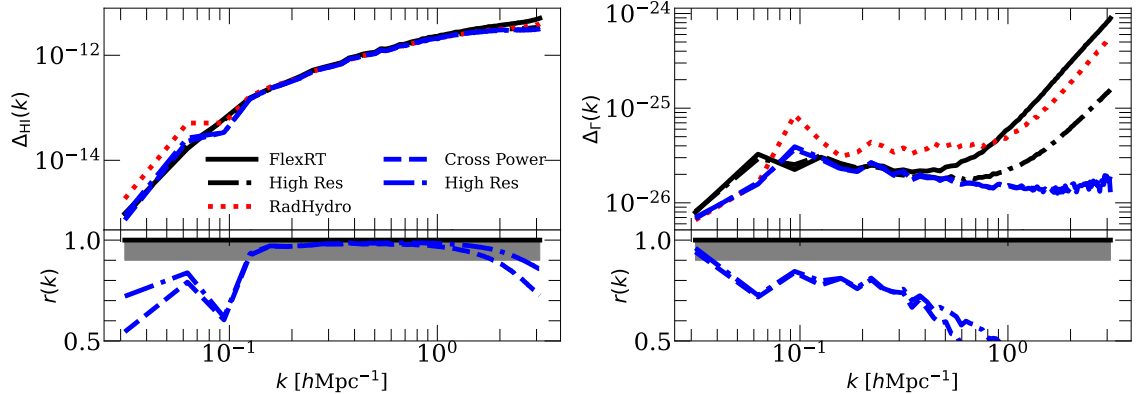


Figure 24. Power spectrum and cross-correlation of the residual x_{HI} (left) and Γ_{HI} (right) fields after the end of reionization. The dot-dashed curves show results for the high-resolution FlexRT run. The bottom panels show $r(k)$. Here, we see significant differences, especially in the Γ_{HI} power. There is more large-scale power at $k < 0.5 h\text{Mpc}^{-1}$ in RADHYDRO, which affects fluctuations in the residual x_{HI} at the largest scales. The higher resolution FlexRT run matches well with the fiducial case at large scales, just with less small-scale noise power.

Fortunately, we have found in previous work [74, 94] that the large-scale fluctuations in the forest are reasonably insensitive to the choice of merging parameters, l_{merge} and N_{ex} . Ref. [94] rigorously quantified this in the context of the IGM opacity/density relation in their Appendix A. The ability to perform such tests easily highlights the flexibility of FLEXRT.

8 Conclusions

We have introduced a new ray-tracing radiative transfer code, FLEXRT, which is aimed at enabling fast, efficient parameter space studies of reionization. FLEXRT combines adaptive ray tracing with a highly flexible treatment of the intergalactic ionizing opacity. This not only gives the user a great deal of control over how the IGM is modeled; it also provides a way to reduce the computational cost of a FLEXRT simulation by orders of magnitude while still modeling the small-scale physics of the IGM. Alternatively, the user may tune up the angular and spatial resolution of the algorithm to run a more traditional reionization simulation.

We have validated FLEXRT against a number of standard test problems common in the literature. We have shown that both the ‘‘Standard’’ and ‘‘Generalized Opacity’’ treatments of the ionizing opacity in FLEXRT are in good agreement with existing codes, given an appropriate prescription for the opacity in the latter. We have run additional tests to validate the accuracy of FLEXRT’s adaptive ray tracing scheme. We find that even when modeling the radiation field with low angular resolution, FLEXRT accurately captures the large-scale growth of ionized regions and the ionizing background fluctuations within them during reionization. Our main conclusions are summarized below:

- We have run the static density field tests described in Paper I of the Cosmological Radiative Transfer Comparison Project [CRTCP, 59]. In Test #1, which models the growth of a spherically symmetric HII region around a point source in a uniform density, isothermal medium, we found excellent agreement between FLEXRT and CRTCP results. We find few-percent level agreement between standard and Generalized Opacity mode in the I-front position, with the latter $< 1\%$ away from the analytic prediction.

- In Test #2, which includes temperature evolution, we find slightly larger ($\sim 10\%$ -level) differences in the temperature profiles in the HII regions, and larger differences in the pre-heating of neutral gas ahead of the I-front. However, our results remain broadly consistent with the CRTCP results.
- Test #3 considers a case where a plane-parallel I-front is shadowed by a dense, partially self-shielding clump. We find good agreement between both modes of FLEXRT and CRTCP codes in the x_{HI} profile in the clump behind the I-front. Generalized Opacity mode fails to capture the ionization and temperature structure in the neutral part of the clump because it does not account for pre-heating, while Standard mode agrees qualitatively with most of the CRTCP codes.
- Finally, Test #4 considers a scenario with multiple sources in a cosmological density field. In this test, we considered only Standard mode, since results from the IFT code (to which Generalized Opacity mode is most comparable) were unavailable. We find broad agreement between Standard mode and the CRTCP codes, but with some differences. The main differences are the use of the finite speed of light in FLEXRT, and the pre-heating of neutral gas by hard ionizing photons. We also compared FLEXRT to RAMSES-RT, which uses the finite speed of light and agrees much better as a result.
- Using a cosmological reionization simulation, we demonstrated the regime in which the moving-screen I-front approximation in Generalized Opacity mode approaches the results of Standard mode. We found that when the RT cell size, Δx_{RT} , is much larger than typical I-front widths, ionization maps from the two modes are almost indistinguishable. Standard mode should be used for problems in which the I-fronts are resolved and their detailed structure is important.
- We validated the ray merging scheme in FLEXRT by repeating CRTCP Test #4 with several sets of merging parameters. We found that lowering the angular resolution of the ray tracing significantly increases shot noise in the radiation field. However, the average ionization fraction and Γ_{HI} , and their large-scale fluctuations, are affected at the 1 – 2% level or less.
- Finally, we tested FLEXRT against the RADHYDRO code of Ref. [47], which uses a similar ray tracing algorithm, in a cosmological reionization simulation. We find good agreement in the morphology of ionized regions and the large-scale fluctuations in Γ_{HI} throughout the bulk of reionization. After the end of reionization, we find modest differences in the in the large-scale Γ_{HI} fluctuations, with $r(k) < 0.7$ at $k > 0.3 h\text{Mpc}^{-1}$. The differences arise due to effects of ray merging, which can be mitigated by adjusting the parameters that control the angular resolution of the radiation field.

The true utility of the Generalized Opacity formalism presented here is to allow for accurate treatments of the IGM opacity when relevant physics (e.g. small-scale clumping and self-shielding) is un-resolved. In the second paper of this series, we will present and validate an improved version of the sub-grid IGM opacity model described in [21, 35, 74].

Acknowledgments

The authors thank Hy Trac for helpful comments on this manuscript and for providing the RADHYDRO code, which inspired much of the ray tracing machinery in FLEXRT. The authors

thank Joakim Rosdahl for providing the RAMSES-RT results for CRTCP Test #4. C.C. acknowledges support from the Beus Center for Cosmic Foundations while this work was being completed. A.D. and C.C. were supported by NASA 19-ATP19-0191 and NSF AST-2045600.

References

- [1] H. Atek, I. Labbé, L.J. Furtak, I. Chemerynska, S. Fujimoto, D.J. Setton et al., *Most of the photons that reionized the Universe came from dwarf galaxies*, *Nature* **626** (2024) 975 [2308.08540].
- [2] A.J. Cameron, H. Katz, C. Witten, A. Saxena, N. Laporte and A.J. Bunker, *Nebular dominated galaxies: insights into the stellar initial mass function at high redshift*, *Monthly Notices of the Royal Astronomical Society* (2024) [2311.02051].
- [3] A. Saxena, A.J. Bunker, G.C. Jones, D.P. Stark, A.J. Cameron, J. Witstok et al., *JADES: The production and escape of ionizing photons from faint Lyman-alpha emitters in the epoch of reionization*, *Astronomy and Astrophysics* **684** (2024) A84 [2306.04536].
- [4] R. Endsley and D.P. Stark, *Strong Lyman- α emission in an overdense region at $z = 6.8$: a very large ($R \approx 3$ physical Mpc) ionized bubble in COSMOS?*, *Monthly Notices of the Royal Astronomical Society* **511** (2022) 6042 [2112.14779].
- [5] L. Whitler, D.P. Stark, R. Endsley, Z. Chen, C. Mason, M.W. Topping et al., *Insight from JWST/Near Infrared Camera into galaxy overdensities around bright Lyman-alpha emitters during reionization: implications for ionized bubbles at $z \approx 9$* , *Monthly Notices of the Royal Astronomical Society* **529** (2024) 855 [2305.16670].
- [6] W.R. Coulton, T. Schutt, A.S. Maniyar, E. Schaan, R. An, Z. Atkins et al., *The Atacama Cosmology Telescope: Detection of Patchy Screening of the Cosmic Microwave Background*, *arXiv e-prints* (2024) arXiv:2401.13033 [2401.13033].
- [7] S. Raghunathan, P.A.R. Ade, A.J. Anderson, B. Ansarinejad, M. Archipley, J.E. Austermann et al., *First Constraints on the Epoch of Reionization Using the non-Gaussianity of the Kinematic Sunyaev-Zeldovich Effect from the South Pole Telescope and Herschel-SPIRE Observations*, *arXiv e-prints* (2024) arXiv:2403.02337 [2403.02337].
- [8] P. Ade, J. Aguirre, Z. Ahmed, S. Aiola, A. Ali, D. Alonso et al., *The Simons Observatory: science goals and forecasts*, *Journal of Cosmology and Astroparticle Physics* **2019** (2019) 056 [1808.07445].
- [9] D. Jain, T.R. Choudhury, S. Raghunathan and S. Mukherjee, *Probing the physics of reionization using kinematic Sunyaev-Zeldovich power spectrum from current and upcoming cosmic microwave background surveys*, *Monthly Notices of the Royal Astronomical Society* **530** (2024) 35 [2311.00315].
- [10] D.R. DeBoer, A.R. Parsons, J.E. Aguirre, P. Alexander, Z.S. Ali, A.P. Beardsley et al., *Hydrogen Epoch of Reionization Array (HERA)*, *Publications of the ASP* **129** (2017) 045001 [1606.07473].
- [11] L. Koopmans, J. Pritchard, G. Mellema, J. Aguirre, K. Ahn, R. Barkana et al., *The Cosmic Dawn and Epoch of Reionisation with SKA*, in *Advancing Astrophysics with the Square Kilometre Array (AASKA14)*, p. 1, Apr., 2015, DOI [1505.07568].
- [12] Z. Abdurashidova, J.E. Aguirre, P. Alexander, Z.S. Ali, Y. Balfour, R. Barkana et al., *HERA Phase I Limits on the Cosmic 21 cm Signal: Constraints on Astrophysics and Cosmology during the Epoch of Reionization*, *The Astrophysical Journal* **924** (2022) 51 [2108.07282].
- [13] HERA Collaboration, Z. Abdurashidova, T. Adams, J.E. Aguirre, P. Alexander, Z.S. Ali et al., *Improved Constraints on the 21 cm EoR Power Spectrum and the X-Ray Heating of the IGM with HERA Phase I Observations*, *The Astrophysical Journal* **945** (2023) 124 [2210.04912].

- [14] G. Kulkarni, L.C. Keating, M.G. Haehnelt, S.E.I. Bosman, E. Puchwein, J. Chardin et al., *Large Ly α opacity fluctuations and low CMB τ in models of late reionization with large islands of neutral hydrogen extending to $z < 5.5$* , *Monthly Notices of the Royal Astronomical Society* **485** (2019) L24 [1809.06374].
- [15] L.C. Keating, G. Kulkarni, M.G. Haehnelt, J. Chardin and D. Aubert, *Constraining the second half of reionization with the Ly β forest*, *Monthly Notices of the Royal Astronomical Society* **497** (2020) 906 [1912.05582].
- [16] F. Nasir and A. D’Aloisio, *Observing the tail of reionization: neutral islands in the $z = 5.5$ Lyman- α forest*, *Monthly Notices of the Royal Astronomical Society* **494** (2020) 3080–3094.
- [17] S.E.I. Bosman, F.B. Davies, G.D. Becker, L.C. Keating, R.L. Davies, Y. Zhu et al., *Hydrogen reionization ends by $z = 5.3$: Lyman- α optical depth measured by the XQR-30 sample*, *Monthly Notices of the Royal Astronomical Society* **514** (2022) 55 [2108.03699].
- [18] Y. Zhu, G.D. Becker, S.E.I. Bosman, L.C. Keating, H.M. Christenson, E. Bañados et al., *Chasing the Tail of Cosmic Reionization with Dark Gap Statistics in the Ly α Forest over $5 < z < 6$* , *The Astrophysical Journal* **923** (2021) 223 [2109.06295].
- [19] Y. Zhu, G.D. Becker, S.E.I. Bosman, L.C. Keating, V. D’Odorico, R.L. Davies et al., *Long Dark Gaps in the Ly β Forest at $z < 6$: Evidence of Ultra-late Reionization from XQR-30 Spectra*, *The Astrophysical Journal* **932** (2022) 76 [2205.04569].
- [20] G.D. Becker, A. D’Aloisio, H.M. Christenson, Y. Zhu, G. Worseck and J.S. Bolton, *The mean free path of ionizing photons at $5 < z < 6$: evidence for rapid evolution near reionization*, *Monthly Notices of the Royal Astronomical Society* **508** (2021) 1853 [2103.16610].
- [21] C. Cain, A. D’Aloisio, N. Gangolli and G.D. Becker, *A Short Mean Free Path at $z = 6$ Favors Late and Rapid Reionization by Faint Galaxies*, *The Astrophysical Journal Letters* **917** (2021) L37 [2105.10511].
- [22] Y. Zhu, G.D. Becker, H.M. Christenson, A. D’Aloisio, S.E.I. Bosman, T. Bakx et al., *Probing Ultralate Reionization: Direct Measurements of the Mean Free Path over $5 < z < 6$* , *The Astrophysical Journal* **955** (2023) 115 [2308.04614].
- [23] P. Gaikwad, M.G. Haehnelt, F.B. Davies, S.E.I. Bosman, M. Molaro, G. Kulkarni et al., *Measuring the photoionization rate, neutral fraction, and mean free path of H I ionizing photons at $4.9 \leq z \leq 6.0$ from a large sample of XShooter and ESI spectra*, *Monthly Notices of the Royal Astronomical Society* **525** (2023) 4093 [2304.02038].
- [24] F.B. Davies, S.E.I. Bosman, P. Gaikwad, F. Nasir, J.F. Hennawi, G.D. Becker et al., *Constraints on the Evolution of the Ionizing Background and Ionizing Photon Mean Free Path at the End of Reionization*, *The Astrophysical Journal* **965** (2024) 134 [2312.08464].
- [25] J.T. Roth, A. D’Aloisio, C. Cain, B. Wilson, Y. Zhu and G.D. Becker, *The effect of reionization on direct measurements of the mean free path*, *Monthly Notices of the Royal Astronomical Society* **530** (2024) 5209 [2311.06348].
- [26] F.B. Davies, J.F. Hennawi, E. Bañados, Z. Lukić, R. Decarli, X. Fan et al., *Quantitative constraints on the reionization history from the IGM damping wing signature in two quasars at $z > 7$* , *The Astrophysical Journal* **864** (2018) 142.
- [27] D. Ďurovčíková, A.-C. Eilers, H. Chen, S. Satyavolu, G. Kulkarni, R.A. Simcoe et al., *Chronicle the Reionization History at $6 \lesssim z \lesssim 7$ with Emergent Quasar Damping Wings*, *The Astrophysical Journal* **969** (2024) 162 [2401.10328].
- [28] LSST Science Collaboration, P.A. Abell, J. Allison, S.F. Anderson, J.R. Andrew, J.R.P. Angel et al., *LSST Science Book, Version 2.0*, *arXiv e-prints* (2009) arXiv:0912.0201 [0912.0201].
- [29] DESI Collaboration, A. Aghamousa, J. Aguilar, S. Ahlen, S. Alam, L.E. Allen et al., *The DESI*

Experiment Part I: Science, Targeting, and Survey Design, *arXiv e-prints* (2016)
arXiv:1611.00036 [1611.00036].

- [30] Y. Zhu, G.D. Becker, S.E.I. Bosman, C. Cain, L.C. Keating, F. Nasir et al., *Damping wing-like features in the stacked Ly α forest: Potential neutral hydrogen islands at $z < 6$* , *Monthly Notices of the Royal Astronomical Society* **533** (2024) L49 [2405.12275].
- [31] B. Spina, S.E.I. Bosman, F.B. Davies, P. Gaikwad and Y. Zhu, *Damping wings in the Lyman- α forest: A model-independent measurement of the neutral fraction at $5.4 < z < 6.1$* , *Astronomy and Astrophysics* **688** (2024) L26 [2405.12273].
- [32] Z. Haiman, T. Abel and P. Madau, *Photon Consumption in Minihalos during Cosmological Reionization*, *The Astrophysical Journal* **551** (2001) 599 [astro-ph/0009125].
- [33] A.R. Duffy, J.S.B. Wyithe, S.J. Mutch and G.B. Poole, *Low-mass galaxy formation and the ionizing photon budget during reionization*, *Monthly Notices of the Royal Astronomical Society* **443** (2014) 3435 [1405.7459].
- [34] F.B. Davies, S.E.I. Bosman, S.R. Furlanetto, G.D. Becker and A. D'Aloisio, *The Predicament of Absorption-dominated Reionization: Increased Demands on Ionizing Sources*, *The Astrophysical Journal Letters* **918** (2021) L35 [2105.10518].
- [35] C. Cain, A. D'Aloisio, N. Gangolli and M. McQuinn, *The morphology of reionization in a dynamically clumpy universe*, *Monthly Notices of the Royal Astronomical Society* **522** (2023) 2047 [2207.11266].
- [36] A.H. Pawlik, J. Schaye and C. Dalla Vecchia, *Spatially adaptive radiation-hydrodynamical simulations of galaxy formation during cosmological reionization*, *Monthly Notices of the Royal Astronomical Society* **451** (2015) 1586 [1501.01980].
- [37] H. Shukla, G. Mellema, I.T. Iliev and P.R. Shapiro, *The effects of Lyman-limit systems on the evolution and observability of the epoch of reionization*, *Monthly Notices of the Royal Astronomical Society* **458** (2016) 135 [1602.01144].
- [38] Y. Mao, J. Koda, P.R. Shapiro, I.T. Iliev, G. Mellema, H. Park et al., *The impact of inhomogeneous subgrid clumping on cosmic reionization*, *Monthly Notices of the Royal Astronomical Society* **491** (2020) 1600 [1906.02476].
- [39] Y. Qin, A. Mesinger, S.E.I. Bosman and M. Viel, *Reionization and galaxy inference from the high-redshift Ly α forest*, *Monthly Notices of the Royal Astronomical Society* **506** (2021) 2390 [<https://academic.oup.com/mnras/article-pdf/506/2/2390/39136191/stab1833.pdf>].
- [40] B. Maity, A. Paranjape and T.R. Choudhury, *A fast method of reionization parameter space exploration using GPR trained SCRIPT*, *Monthly Notices of the Royal Astronomical Society* **526** (2023) 3920 [2305.04839].
- [41] S.R. Furlanetto, M. Zaldarriaga and L. Hernquist, *The Growth of H II Regions During Reionization*, *The Astrophysical Journal* **613** (2004) 1 [astro-ph/0403697].
- [42] A. Mesinger and S. Furlanetto, *Efficient Simulations of Early Structure Formation and Reionization*, *The Astrophysical Journal* **669** (2007) 663 [0704.0946].
- [43] B. Greig and A. Mesinger, *21CMMC: an MCMC analysis tool enabling astrophysical parameter studies of the cosmic 21 cm signal*, *Monthly Notices of the Royal Astronomical Society* **449** (2015) 4246 [1501.06576].
- [44] T.R. Choudhury and A. Paranjape, *Photon number conservation and the large-scale 21 cm power spectrum in seminumerical models of reionization*, *Monthly Notices of the Royal Astronomical Society* **481** (2018) 3821 [1807.00836].
- [45] H. Trac, N. Chen, I. Holst, M.A. Alvarez and R. Cen, *AMBER: A Semi-numerical Abundance Matching Box for the Epoch of Reionization*, *The Astrophysical Journal* **927** (2022) 186 [2109.10375].

- [46] G. Mellema, I.T. Iliev, M.A. Alvarez and P.R. Shapiro, *C²-ray: A new method for photon-conserving transport of ionizing radiation*, *New Astronomy* **11** (2006) 374 [[astro-ph/0508416](#)].
- [47] H. Trac and R. Cen, *Radiative transfer simulations of cosmic reionization. i. methodology and initial results*, *The Astrophysical Journal* **671** (2007) 1.
- [48] J. Rosdahl, J. Blaizot, D. Aubert, T. Stranex and R. Teyssier, *RAMSES-RT: radiation hydrodynamics in the cosmological context*, *Monthly Notices of the Royal Astronomical Society* **436** (2013) 2188 [[1304.7126](#)].
- [49] N.Y. Gnedin, *Cosmic Reionization on Computers. I. Design and Calibration of Simulations*, *The Astrophysical Journal* **793** (2014) 29 [[1403.4245](#)].
- [50] P. Ocvirk, N. Gillet, P.R. Shapiro, D. Aubert, I.T. Iliev, R. Teyssier et al., *Cosmic Dawn (CoDa): the First Radiation-Hydrodynamics Simulation of Reionization and Galaxy Formation in the Local Universe*, *Monthly Notices of the Royal Astronomical Society* **463** (2016) 1462 [[1511.00011](#)].
- [51] J. Rosdahl, H. Katz, J. Blaizot, T. Kimm, L. Michel-Dansac, T. Garel et al., *The SPHINX cosmological simulations of the first billion years: the impact of binary stars on reionization*, *Monthly Notices of the Royal Astronomical Society* **479** (2018) 994 [[1801.07259](#)].
- [52] R. Kannan, E. Garaldi, A. Smith, R. Pakmor, V. Springel, M. Vogelsberger et al., *Introducing the THESAN project: radiation-magnetohydrodynamic simulations of the epoch of reionization*, *Monthly Notices of the Royal Astronomical Society* **511** (2022) 4005 [[2110.00584](#)].
- [53] O. Zahn, A. Mesinger, M. McQuinn, H. Trac, R. Cen and L.E. Hernquist, *Comparison of reionization models: radiative transfer simulations and approximate, seminumeric models*, *Monthly Notices of the Royal Astronomical Society* **414** (2011) 727 [[1003.3455](#)].
- [54] Y. Qin, J.S.B. Wyithe, P.A. Oesch, G.D. Illingworth, E. Leonova, S.J. Mutch et al., *Dark-ages reionization and galaxy formation simulation XX. The Ly α IGM transmission properties and environment of bright galaxies during the epoch of reionization*, *Monthly Notices of the Royal Astronomical Society* **510** (2022) 3858 [[2108.03675](#)].
- [55] P. Ocvirk, D. Aubert, J.G. Sorce, P.R. Shapiro, N. Deparis, T. Dawoodbhoy et al., *Cosmic Dawn II (CoDa II): a new radiation-hydrodynamics simulation of the self-consistent coupling of galaxy formation and reionization*, *Monthly Notices of the Royal Astronomical Society* **496** (2020) 4087 [[1811.11192](#)].
- [56] A. Doussot, H. Trac and R. Cen, *SCORCH. II. Radiation-hydrodynamic Simulations of Reionization with Varying Radiation Escape Fractions*, *The Astrophysical Journal* **870** (2019) 18 [[1712.04464](#)].
- [57] M. Vogelsberger, S. Genel, V. Springel, P. Torrey, D. Sijacki, D. Xu et al., *Introducing the illustris project: simulating the coevolution of dark and visible matter in the universe*, *Monthly Notices of the Royal Astronomical Society* **444** (2014) 1518.
- [58] S. Hassan, R. Davé, M. McQuinn, R.S. Somerville, L.C. Keating, D. Anglés-Alcázar et al., *Reionization with SIMBA: How Much Does Astrophysics Matter in Modeling Cosmic Reionization?*, *The Astrophysical Journal* **931** (2022) 62 [[2109.03840](#)].
- [59] I.T. Iliev, B. Ciardi, M.A. Alvarez, A. Maselli, A. Ferrara, N.Y. Gnedin et al., *Cosmological radiative transfer codes comparison project - I. The static density field tests*, *Monthly Notices of the Royal Astronomical Society* **371** (2006) 1057 [[astro-ph/0603199](#)].
- [60] Planck Collaboration, N. Aghanim, Y. Akrami, M. Ashdown, J. Aumont, C. Baccigalupi et al., *Planck 2018 results. VI. Cosmological parameters*, *Astronomy and Astrophysics* **641** (2020) A6 [[1807.06209](#)].

- [61] C. Levermore, *Relating eddington factors to flux limiters*, *Journal of Quantitative Spectroscopy and Radiative Transfer* **31** (1984) 149.
- [62] N.Y. Gnedin and T. Abel, *Multi-dimensional cosmological radiative transfer with a Variable Eddington Tensor formalism*, *New Astronomy* **6** (2001) 437 [[astro-ph/0106278](#)].
- [63] I.T. Iliev, D. Whalen, G. Mellema, K. Ahn, S. Baek, N.Y. Gnedin et al., *Cosmological radiative transfer comparison project - II. The radiation-hydrodynamic tests*, *Monthly Notices of the Royal Astronomical Society* **400** (2009) 1283 [[0905.2920](#)].
- [64] R. Kannan, M. Vogelsberger, F. Marinacci, R. McKinnon, R. Pakmor and V. Springel, *AREPO-RT: radiation hydrodynamics on a moving mesh*, *Monthly Notices of the Royal Astronomical Society* **485** (2019) 117 [[1804.01987](#)].
- [65] X. Wu, M. McQuinn and D. Eisenstein, *On the accuracy of common moment-based radiative transfer methods for simulating reionization*, *Journal of Cosmology and Astroparticle Physics* **2021** (2021) 042 [[2009.07278](#)].
- [66] P. Hirling, M. Bianco, S.K. Giri, I.T. Iliev, G. Mellema and J.P. Kneib, *pyC2Ray: A flexible and GPU-accelerated radiative transfer framework for simulating the cosmic epoch of reionization*, *Astronomy and Computing* **48** (2024) 100861 [[2311.01492](#)].
- [67] T. Abel and B.D. Wandelt, *Adaptive ray tracing for radiative transfer around point sources*, *Monthly Notices of the Royal Astronomical Society* **330** (2002) L53 [[astro-ph/0111033](#)].
- [68] M. McQuinn, A. Lidz, O. Zahn, S. Dutta, L. Hernquist and M. Zaldarriaga, *The morphology of HII regions during reionization*, *Monthly Notices of the Royal Astronomical Society* **377** (2007) 1043 [[astro-ph/0610094](#)].
- [69] B. Hartley and M. Ricotti, *ARC: adaptive ray-tracing with CUDA, a new ray tracing code for parallel GPUs*, *Monthly Notices of the Royal Astronomical Society* **483** (2019) 1582 [[1807.07094](#)].
- [70] Z. Zheng, R. Cen, H. Trac and J. Miralda-Escudé, *Radiative Transfer Modeling of Ly α Emitters. I. Statistics of Spectra and Luminosity*, *The Astrophysical Journal* **716** (2010) 574 [[0910.2712](#)].
- [71] E. Visbal and M. McQuinn, *The Impact of Neutral Intergalactic Gas on Ly α Intensity Mapping during Reionization*, *The Astrophysical Journal Letters* **863** (2018) L6 [[1807.03370](#)].
- [72] B. Ciardi, A. Ferrara, S. Marri and G. Raimondo, *Cosmological reionization around the first stars: Monte Carlo radiative transfer*, *Monthly Notices of the Royal Astronomical Society* **324** (2001) 381 [[astro-ph/0005181](#)].
- [73] A. Maselli, A. Ferrara and B. Ciardi, *CRASH: a radiative transfer scheme*, *Monthly Notices of the Royal Astronomical Society* **345** (2003) 379 [[astro-ph/0307117](#)].
- [74] C. Cain, A. D’Aloisio, G. Lopez, N. Gangolli and J.T. Roth, *On the rise and fall of galactic ionizing output at the end of reionization*, *Monthly Notices of the Royal Astronomical Society* **531** (2024) 1951 [[2311.13638](#)].
- [75] K.M. Gorski, B.D. Wandelt, F.K. Hansen, E. Hivon and A.J. Banday, *The HEALPix Primer*, *arXiv e-prints* (1999) astro [[astro-ph/9905275](#)].
- [76] A. Sokasian, T. Abel and L.E. Hernquist, *Simulating reionization in numerical cosmology*, *New Astronomy* **6** (2001) 359 [[astro-ph/0105181](#)].
- [77] B. Wilson, A. D’Aloisio, G.D. Becker, C. Cain and E. Visbal, *Quantifying Lyman- α emissions from reionization fronts*, *arXiv e-prints* (2024) arXiv:2406.14622 [[2406.14622](#)].
- [78] L. Hui and N.Y. Gnedin, *Equation of state of the photoionized intergalactic medium*, *Monthly Notices of the Royal Astronomical Society* **292** (1997) 27 [[astro-ph/9612232](#)].

- [79] J.D. Emberson, R.M. Thomas and M.A. Alvarez, *THE OPACITY OF THE INTERGALACTIC MEDIUM DURING REIONIZATION: RESOLVING SMALL-SCALE STRUCTURE*, *The Astrophysical Journal* **763** (2013) 146.
- [80] H. Park, P.R. Shapiro, J.-h. Choi, N. Yoshida, S. Hirano and K. Ahn, *The Hydrodynamic Feedback of Cosmic Reionization on Small-scale Structures and Its Impact on Photon Consumption During the Epoch of Reionization*, *ApJ* **831** (2016) 86 [1602.06472].
- [81] A. D’Aloisio, M. McQuinn, H. Trac, C. Cain and A. Mesinger, *Hydrodynamic response of the intergalactic medium to reionization*, *The Astrophysical Journal* **898** (2020) 149.
- [82] T.K. Chan, A. Benítez-Llambay, T. Theuns, C. Frenk and R. Bower, *The impact and response of mini-haloes and the interhalo medium on cosmic reionization*, *Monthly Notices of the Royal Astronomical Society* **528** (2024) 1296 [2305.04959].
- [83] A. D’Aloisio, M. McQuinn, O. Maupin, F.B. Davies, H. Trac, S. Fuller et al., *Heating of the Intergalactic Medium by Hydrogen Reionization*, *The Astrophysical Journal* **874** (2019) 154 [1807.09282].
- [84] C. Zeng and C.M. Hirata, *Nonequilibrium Temperature Evolution of Ionization Fronts during the Epoch of Reionization*, *The Astrophysical Journal* **906** (2021) 124 [2007.02940].
- [85] H. Susa and T. Kitayama, *Collapse of low-mass clouds in the presence of a UV radiation field*, *Monthly Notices of the Royal Astronomical Society* **317** (2000) 175 [astro-ph/0004303].
- [86] T. Nakamoto, M. Umemura and H. Susa, *The effects of radiative transfer on the reionization of an inhomogeneous universe*, *Monthly Notices of the Royal Astronomical Society* **321** (2001) 593.
- [87] A.O. Razoumov and C.Y. Cardall, *Fully threaded transport engine: new method for multi-scale radiative transfer*, *Monthly Notices of the Royal Astronomical Society* **362** (2005) 1413 [astro-ph/0505172].
- [88] J. Ritzerveld, V. Icke and E.-J. Rijkhorst, *Triangulating Radiation: Radiative Transfer on Unstructured Grids*, *arXiv e-prints* (2003) astro [astro-ph/0312301].
- [89] D. Whalen and M.L. Norman, *A Multistep Algorithm for the Radiation Hydrodynamical Transport of Cosmological Ionization Fronts and Ionized Flows*, *The Astrophysical Journal Supplement* **162** (2006) 281 [astro-ph/0508214].
- [90] E.J. Rijkhorst, T. Plewa, A. Dubey and G. Mellema, *Hybrid characteristics: 3D radiative transfer for parallel adaptive mesh refinement hydrodynamics*, *Astronomy and Astrophysics* **452** (2006) 907 [astro-ph/0505213].
- [91] M.A. Alvarez, V. Bromm and P.R. Shapiro, *The H II Region of the First Star*, *The Astrophysical Journal* **639** (2006) 621 [astro-ph/0507684].
- [92] S.L. Finkelstein, A. D’Aloisio, J.-P. Paardekooper, J. Ryan, Russell, P. Behroozi, K. Finlator et al., *Conditions for Reionizing the Universe with a Low Galaxy Ionizing Photon Escape Fraction*, *The Astrophysical Journal* **879** (2019) 36 [1902.02792].
- [93] F.B. Davies and S.R. Furlanetto, *Large fluctuations in the hydrogen-ionizing background and mean free path following the epoch of reionization*, *Monthly Notices of the Royal Astronomical Society* **460** (2016) 1328 [1509.07131].
- [94] N. Gangolli, A. D’Aloisio, C. Cain, G.D. Becker and H. Christenson, *On the correlation between Ly α forest opacity and galaxy density in late reionization models*, *arXiv e-prints* (2024) arXiv:2408.08358 [2408.08358].